



ELSEVIER

Contents lists available at ScienceDirect

Computer Methods in Applied Mechanics and Engineering

journal homepage: www.elsevier.com/locate/cma

Peridynamic modeling of elastic-plastic ductile fracture

Heng Zhang^{a,*}, Dan Huang^a, Xiong Zhang^b^a Department of Engineering Mechanics, Hohai University, Nanjing 210098, China^b School of Aerospace Engineering, Tsinghua University, Beijing 100084, China

HIGHLIGHTS

- A peridynamics-based framework is established for elastic-plastic ductile fracture problems.
- Energy dissipation rate-based bond failure criterion is proposed for ductile crack growth modeling.
- The peridynamic models successfully capture the characteristics of elastic-plastic deformation and ductile fracture.

ARTICLE INFO

Keywords:

Peridynamics
Elastic-plastic materials
Ductile fracture
Crack growth modeling

ABSTRACT

A peridynamics-based framework is established for the elastic-plastic ductile fracture analysis. In this frame, a new state-based peridynamic elastic-plastic model is presented using the novel bond extension state forms of yield function and plastic flow rule. The nonlinear energy release rate is computed by the extended peridynamic finite crack extension (PFCE) method, and an energy dissipation rate-based bond failure criterion is proposed for ductile crack growth modeling. Numerical methods for plastic states update and yield function solution are also given. Then, examples of plates with a center hole or a center crack, and compact tension (CT) tests are analyzed by the proposed models, and compared to those from theoretical and FEM solutions. The results demonstrate that the proposed peridynamic models can well capture the characteristics of elastic-plastic deformation and ductile fracture, including the plastic shape and size, energy distributions, nonlinear energy release rate, load-displacement and resistance curves, etc.

1. Introduction

Crack growth in ductile materials commonly experiences material plastic deformations, which leads to elastic-plastic fracture. The better understanding and prediction of elastic-plastic ductile fracture are important for the fracture resistance quantification of ductile materials and structures.

In elastic-plastic fracture mechanics, the most widely accepted parameter, J-integral [1,2] has been proposed to measure the stress and strain fields of crack-tip and characterize the crack initiation. The J-integral was later extended for crack growth problems with the so-called J-resistance curve [3]. However, the J-integral is only applicable for small-scale yielding problems with limited crack extension length. A physical more meaningful parameter of energy dissipation rate R [4,5], defined as the summation of the unrecoverable plastic energy rate and the crack surface separation energy rate, was utilized to analyze ductile crack growth problems. Meanwhile, the numerical Finite Element Method (FEM) model has great advantage on plastic deformation analysis, with which the J-integral value of stationary cracks can be computed. The FEM model has also been used for ductile crack growth analysis with

* Corresponding author.

E-mail address: hengzh@hhu.edu.cn (H. Zhang).

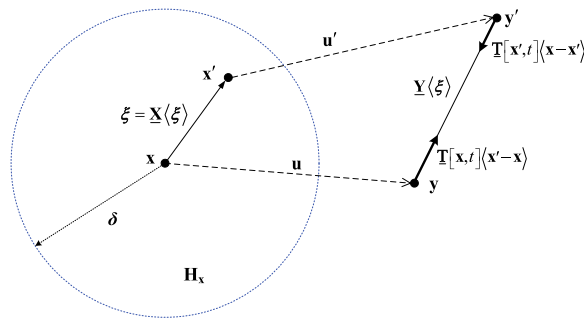


Fig. 1. Ordinary state-based peridynamic model.

incorporating the cohesive zone model (CZM) [6], continuum damage model [7], virtual crack extension method [8], and phase-field models [9,10]. However, it is still great challenge to fully model the elastic-plastic ductile fracture problem because of the interaction between material plasticity and crack growth.

Peridynamic (PD) [11] was proposed as a reformulation of classical mechanics to solve fracture problems. In peridynamics, the classical partial differential equations are replaced with integral differential equations, and the inadequacies of continuous mechanics on fracture problems can be removed. Thus, peridynamics can naturally model fracture problems of crack initiation and propagation. The original version of peridynamic theory is bond-based peridynamic (BB-PD) model, where the bond force interacted with neighboring points depends only on their own deformations. This leads to restrictions of Poisson’s ratio for BB-PD model [12]. To handle such restrictions, a more general frame of the state-based peridynamic (SB-PD) model [13] was proposed, in which the bond force density between neighboring points depends on the deformation of their whole family. The SB-PD can be further divided into ordinary and non-ordinary models. In ordinary state-based peridynamics (OSB-PD) [13], the bond force density is parallel to the bond deformed vector; while in non-ordinary state-based peridynamics (NOSB-PD) [14,15], the bond force is not limited to be parallel to the bond deformed vector. Based on these peridynamic models, different materials in conventional solid mechanics were reformulated [16–22].

To reproduce the plastic deformations, peridynamics-based plastic models were successively proposed. The concept of peridynamic elastic-plastic model was first presented in [13] with the frame of OSB-PD. It was later extended as a three-dimensional (3D) peridynamic perfect elastic-plastic model with the non-local yield criterion [23]. The OSB-PD constitutive plastic model based on von Mises yield criteria with isotropic hardening was proposed in [24], for both 1D, 2D and 3D cases. This model was extensively studied with isotropic, kinematic and mixed hardenings under cyclic loading [25]. To model the geomaterials and concrete, the nonlocal peridynamic plastic models were derived based on the Drucker-Prager criterion and the pressure-dependent non-associated flow rule [26–30]. For typical 2D elastoplastic case, a new 2D OSB-PD model consistent with J2 plasticity was proposed using a novel decomposition for force and extension states [31]. Additionally, the NOSB-PD based plastic models [32–34] were also formulated for plastic deformation analysis. But, the zero-energy mode exists in the NOSB-PD model [35,36], which may cause the unstable solutions. Overall, most above researches are only related to plastic deformations analysis. Though the equivalent Mises stress and equivalent plastic strain around stationary cracks were presented in some studies [27,37,38], the elastic-plastic ductile crack growth is rarely modeled.

Bond failure criterion is important in peridynamic theory for fracture analysis. The most common two are critical stretch (CS) and critical energy density (CED) criteria. The CS bond failure criterion was first proposed in the BB-PD model [12], and extended in the OSB-PD model [39]. But the CS-based bond failure criterion can only be used for elastic brittle fracture. For the plastic ductile fracture, since the relationship between the bond force and bond deformation is nonlinear and history dependent, the CS criterion cannot be utilized. The CED criterion related to deformation states was first proposed by Foster et al. [40]. It was extended for crack elastic-plastic growth modeling in [24], where the critical CED in [24,40] is still computed from critical energy release rate. However, in ductile fracture problem, the critical energy release rate involves not only surface fracture energy but also global plastic energy, the plastic energy dissipation effect has not been clearly considered in [24,40]. Additionally, there is few studies on quantitative analysis of elastic-plastic ductile fracture behaviors, i.e. the plastic shape and size, energy distributions, nonlinear energy release rate, load-displacement and resistance curves, etc.

In the present study, the peridynamics-based framework is established for the elastic-plastic ductile fracture analysis. First, the ordinary state-based peridynamic elastic-plastic model is presented for elastic-plastic deformations analysis, in which the yield function and plastic flow rule are defined only with the bond extension states. Then, the nonlinear energy release rate of crack is computed by extended peridynamic finite crack extension (PFCE) method, and an energy dissipation rate-based bond energy density criterion is proposed for ductile crack growth modeling. Numerical methods of plastic deformation states update and yield function solution are given. Examples of plates with a center hole or a center crack, and compact tension (CT) tests, are analyzed for the model verification and application, and δ -convergence and m -convergence studies are performed. The elastic-plastic deformation and fracture behaviors of these tests are predicted with the proposed models, and compared to those from analytical and FEM results.

2. Elastic-plastic model in ordinary state-based peridynamics

In nonlocal peridynamic theory, the motion equation of the peridynamic point \mathbf{x} can be expressed as [3]:

$$\rho(\mathbf{x})\ddot{\mathbf{u}}(\mathbf{x}, t) = \int_{H_{\mathbf{x}}} \left\{ \mathbb{T}[\mathbf{x}, t](\mathbf{x}' - \mathbf{x}) - \mathbb{T}[\mathbf{x}', t](\mathbf{x} - \mathbf{x}') \right\} dV_{\mathbf{x}'} + \mathbf{b}(\mathbf{x}, t) \quad (1)$$

where ρ is the density of point \mathbf{x} , \mathbf{u} is the displacement vector at time t , $H_{\mathbf{x}}$ is the neighborhood of point \mathbf{x} with the nonlocal horizon size of δ , \mathbf{x}' is its neighbor point in $H_{\mathbf{x}}$, and $\mathbf{b}(\mathbf{x}, t)$ is the body force density. As shown in Fig. 1, $\xi = \mathbf{x}' - \mathbf{x}$ is the bond vector, $\underline{\mathbf{X}}(\xi)$ and $\underline{\mathbf{Y}}(\xi)$ are the reference and deformed vectors of bond ξ , $\mathbb{T}[\mathbf{x}, t]$ and $\mathbb{T}[\mathbf{x}', t]$ are the force vector states of points \mathbf{x} and \mathbf{x}' , respectively.

In the ordinary state-based peridynamic (OSB-PD) model, the bond force is parallel to the bond deformed vector, and it can be written with the force scalar state \underline{t} as:

$$\mathbb{T}[\mathbf{x}, t](\xi) = \underline{t}(\xi) \frac{\underline{\mathbf{Y}}(\xi)}{|\underline{\mathbf{Y}}(\xi)|} \quad (2)$$

2.1. Peridynamic model for elastic deformation

In the peridynamic elastic-plastic model, the bond deformation can be decomposed as:

$$\underline{e} = \underline{e}^j + \underline{e}^{de} + \underline{e}^{dp} \quad (3)$$

where \underline{e} is the extension scalar state defined as $\underline{e} = |\underline{\mathbf{Y}}| - |\underline{\mathbf{X}}|$, \underline{e}^j , \underline{e}^{de} and \underline{e}^{dp} are the volume, elastic and plastic deviatoric parts of extension scalar state, respectively. Thus, the elastic deviatoric extension \underline{e}^{de} can be computed with the nonlocal volume dilatation θ for the three-dimensional (3D) and two-dimensional (2D) cases as:

$$\begin{cases} \theta = 3 \frac{\omega \underline{x} \cdot \underline{e}}{q}, \underline{e}^{de} = \underline{e} - \frac{\theta}{3} \underline{x} - \underline{e}^{dp}; & 3\text{D} \\ \theta = 2 \frac{\omega \underline{x} \cdot \underline{e}}{q}, \underline{e}^{de} = \underline{e} - \frac{\theta}{2} \underline{x} - \underline{e}^{dp}; & 2\text{D} \end{cases} \quad (4)$$

For isotropic materials, the elastic strain energy density of point \mathbf{x} in the OSB-PD model can be expressed as:

$$W_e = \frac{k\theta^2}{2} + \frac{\alpha}{2} \left(\omega e^{de} \right) \cdot \underline{e}^{de} \quad (5)$$

where k and α are the peridynamic constants, which can be expressed as:

$$\begin{cases} k = k', \alpha = \frac{15\mu}{q}; & 3\text{D} \\ k = k', \alpha = \frac{8\mu}{q}; & 2\text{D} \end{cases} \quad (6)$$

Thus, the scalar force state \underline{t} takes the form of [39]:

$$\underline{t} = \begin{cases} 3k' \theta \frac{\omega \underline{x}}{q} + \frac{15\mu}{q} \omega e^{de} & 3\text{D} \\ 2k' \theta \frac{\omega \underline{x}}{q} + \frac{8\mu}{q} \omega e^{de} & 2\text{D} \end{cases} \quad (7)$$

where \underline{x} is the scalar state of bond ξ that is equal to the bond length $|\xi|$, ω is the influence function, q is the weighted volume that is defined as $\omega \underline{x} \cdot \underline{x}$, the symbol (\cdot) is dot product in [3], μ is the shear modulus, and k' is the modulus that can be expressed with the Young's modulus E and Poisson's ratio ν in 3D and 2D cases as:

$$k' = \begin{cases} \frac{E}{3(1-2\nu)} & 3\text{D} \\ \frac{E}{2(1-\nu)} & \text{Plane stress} \\ \frac{E}{2(1+\nu)(1-2\nu)} & \text{Plane strain} \end{cases} \quad (8)$$

2.2. Strain energy density decomposition

The elastic strain energy density in Eq. (5) can be decomposed into volumetric and distortional strain energy density as:

$$W_e = W^v + W^d \quad (9)$$

where the volumetric part of elastic energy density in classical mechanics is

$$W^v = \frac{1}{2}K \left(\frac{dV}{V} \right)^2 \quad (10)$$

where K is the bulk modulus for the 3D case, dV/V is the volumetric strain that can be computed with the nonlocal volume dilatation θ as:

$$\frac{dV}{V} = \begin{cases} \theta & \text{3D} \\ \frac{1-2\nu}{1-\nu} \theta & \text{Plane stress} \\ \theta & \text{Plane strain} \end{cases} \quad (11)$$

Substitute Eq. (11) into Eq. (10), and consider 3D bulk modulus $K = E / (3-6\nu)$, the volumetric strain energy density in peridynamics can be expressed as:

$$W^v = \begin{cases} \frac{E}{6(1-2\nu)} \theta^2 & \text{3D} \\ \frac{E(1-2\nu)}{6(1-\nu)^2} \theta^2 & \text{Plane stress} \\ \frac{E}{6(1-2\nu)} \theta^2 & \text{Plane strain} \end{cases} \quad (12)$$

Combine Eqs. (5), (9) and (12), the distortional strain energy density in peridynamics can be obtained as:

$$W^d = \begin{cases} \frac{15\mu}{2q} \left(\underline{\omega e^{de}} \right) \cdot \underline{e^{de}} & \text{3D} \\ \frac{E(1+\nu)}{12(1-\nu)^2} \theta^2 + \frac{4\mu}{q} \left(\underline{\omega e^{de}} \right) \cdot \underline{e^{de}} & \text{Plane stress} \\ \frac{E}{12(1+\nu)} \theta^2 + \frac{4\mu}{q} \left(\underline{\omega e^{de}} \right) \cdot \underline{e^{de}} & \text{Plane strain} \end{cases} \quad (13)$$

Thus, the forms of volumetric and distortional strain energy density in peridynamics are, respectively given in Eqs (12) and (13), which are strictly equivalent to the volumetric and distortional strain energy density in classical mechanics for both 2D and 3D cases. As shown in Eq (13), in the 3D case, W^d is only a function of the elastic deviatoric extension $\underline{e^{de}}$. While in the 2D case, W^d is the function of both $\underline{e^{de}}$ and the volume dilatation θ , which is different to the deviatoric strain energy density definition in [3].

2.3. Yield function and plastic flow rule

According to the classical J2 plasticity theory, the distortional strain energy density-based yield function can be presented as:

$$f(W^d) = W^d - \psi \quad (14)$$

where W^d is the distortional strain energy density given in Eq. (13), ψ is a positive hardening variable that is related to deformation history. For the linear isotropic strain hardening model, ψ can be expressed as:

$$\psi = \frac{(\sigma_Y + H\varepsilon_p)^2}{6\mu} \quad (15)$$

where σ_Y is the yield stress, ε_p is the equivalent plastic strain, μ is the shear modulus, and H is the hardening modulus. When $H = 0$ is considered, ψ is a constant, the yield function is responding to the perfectly elastic-plastic materials.

When the yield condition is reached, the plastic flow rule is needed to update the plastic part of bond extension. The plastic flow rule is considered as [23]:

$$\Delta \underline{e^{dp}} = \lambda \nabla^d (W^d) \quad (16)$$

where $\Delta \underline{e^{dp}}$ is the increment plastic deviatoric extension scalar state, λ is the positive undetermined scalar parameter, and ∇^d is Frechet

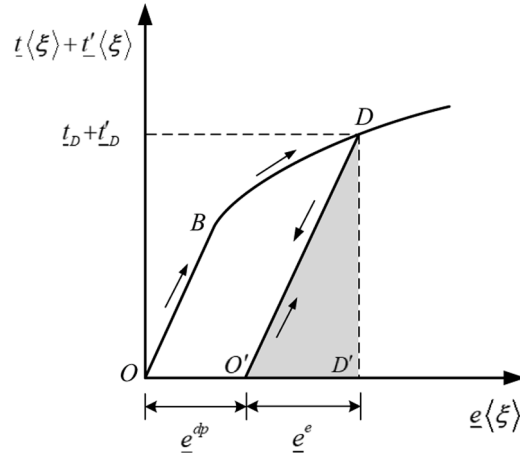


Fig. 2. The bond force related to bond extension scalar in peridynamic elastic-plastic model.

derivative of W^d with respect to e^{de} . Substitute Eq. (13) into Eq. (16), the plastic flow rule can be rewritten as:

$$\Delta e^{dp} = \begin{cases} \lambda \frac{15\mu}{q} \omega e^{de} & 3D \\ \lambda \frac{8\mu}{q} \omega e^{de} & 2D \end{cases} \quad (17)$$

where $\nabla^d(\theta) = 0$ is used. Using this form of flow rule, the increment plastic extension Δe^{dp} can be directly computed by the elastic deviatoric extension e^{de} with the undetermined scalar parameter λ .

Unlike the previous peridynamic elastic-plastic models in [23,24,31], the present yield function of Eq. (14) and plastic flow rule of Eq. (17) are defined only with the bond elastic deviatoric extension e^{de} , no bond force state is involved. It would reduce the numerical solution difficulty of present peridynamic elastic-plastic model, especially for the 2D plane stress and strain cases, which would be shown in the numerical implementation section.

2.4. Equivalent Mises stress and equivalent plastic strain

Based on the classical J2 theory, the equivalent Mises stress of the peridynamic point is defined as:

$$\sigma_M = \sqrt{6\mu W^d} \quad (18)$$

where W^d is the distortional strain energy density, μ is the shear modulus. Using the forms of W^d in Eq. (13), the equivalent Mises stress can be obtained in both the 3D and 2D cases.

Meanwhile, the equivalent plastic strain ε_p is related to point deformation history, the increment equivalent plastic strain can be computed by [37,41]:

$$\Delta \varepsilon^p = \begin{cases} \sqrt{\frac{5}{q} \left(\omega \Delta e^{dp} \right) \cdot \Delta e^{dp}} & 3D \\ \sqrt{\frac{2}{q} \left(\omega \Delta e^{dp} \right) \cdot \Delta e^{dp}} & 2D \end{cases} \quad (19)$$

where q is the weighted volume, Δe^{dp} is the increment plastic deviatoric extension scalar state computed by Eq. (17).

3. Elastic-plastic fracture in peridynamics

In this section, the nonlinear energy release rate of elastic-plastic crack is computed by the extended peridynamic finite crack extension (PFCE) method. An energy dissipation rate-based bond energy density criterion is proposed for the elastic-plastic ductile crack growth modeling.

3.1. Elastic-plastic bond energy density

In the ordinary peridynamic elastic-plastic model, the curve of bond force scalar $\underline{t}(\xi) + \underline{t}'(\xi)$ related to bond extension scalar $\underline{e}(\xi)$ can be approximately plotted in Fig. 2. As shown, the bond force firstly linearly increases with the bond extension from point O to B , and then encounters nonlinear elastic behavior from B to D as the point yield function is satisfied. If the unloading occurs at the point D , the bond force would decrease elastically from point D to O' , and follow the same reloading curve when the load is applied again.

As shown in Fig. 2, under the elastic-plastic deformation, the bond extension $\underline{e}(\xi)$ can be divided into two parts: the elastic extension $\underline{e}^e = \underline{e}^i + \underline{e}^{de}$ and the unrecoverable plastic extension \underline{e}^{dp} . Thus, the bond energy density $\underline{w}(\xi)$ can also be divided as the sum of the elastic energy density \underline{w}^e and plastic energy density \underline{w}^p . The value of elastic bond energy \underline{w}^e is equal to area of the triangle $O'DD'$, that can be computed by:

$$\underline{w}^e(\xi) = \frac{1}{2} \left\{ \underline{t}_D(\xi) + \underline{t}'_D(\xi) \right\} \cdot \underline{e}^e(\xi) \quad (20)$$

The value of plastic bond energy density \underline{w}^p is equal to area of $OBD O'$, that can only be computed in the integral form:

$$\underline{w}^p(\xi) = \int_0^{\underline{e}^{dp}(\xi)} \left\{ \underline{t}(\xi) + \underline{t}'(\xi) \right\} \cdot d\underline{e}^{dp}(\xi) \quad (21)$$

Based on the definitions of these bond energy densities, the elastic and plastic strain energy density of the peridynamic point \mathbf{x} can be computed by:

$$\begin{aligned} W_e &= \int_{H_\xi} \frac{1}{2} \underline{w}^e(\xi) dV_\xi \\ W_p &= \int_{H_\xi} \frac{1}{2} \underline{w}^p(\xi) dV_\xi \end{aligned} \quad (22)$$

3.2. Nonlinear energy release rate computation in peridynamics

The nonlinear energy release rate (NERR) J is a significant parameter to characterize the crack in the elastic-plastic fracture problem, which is proved equal to path-independent contour J-integral in a nonlinear elastic body [42]. Here, the peridynamic finite crack extension (PFCE) method [43] is extended for the J computation.

In elastic-plastic solid materials, for a crack difference of dA , the energy variations of the system must satisfy [44]:

$$dW_F = dU_e + dU_p + dU_k + dW_s \quad (23)$$

where W_F is the total potential of the external force, U_e is the elastic strain energy, U_p is the plastic strain energy, U_k is the kinetic energy, and W_s is the crack surface energy. For quasi-static problems, U_k can be neglected. The nonlinear energy release rate during elastic-plastic crack growth can be expressed as:

$$J = \frac{dW_F - (dU_e + dU_p)}{dA} \quad (24)$$

Considering the fixed displacement boundary conditions, the Eq. (24) can be rewritten as:

$$J = \frac{-(dU_e + dU_p)}{dA} \quad (25)$$

Thus, the nonlinear energy release rate J of an elastic-plastic crack can be computed by the differential of the total strain energy to the crack area, which can be numerically calculated with the total strain energy difference by specimens with neighboring crack sizes.

In the peridynamic elastic-plastic model, after calculating the total strain energy of specimens with neighboring crack sizes, numerical differentiation is utilized to obtain the value of J , where the elastic and plastic strain energy of peridynamic points can be computed by Eq. (22). Additionally, unlike the original PFCE method for elastic materials [43], which can be solved by one specimen with series artificial crack extensions; for the elastic-plastic materials, since previous plastic energy would remain when crack extensions are artificially applied, the extended PFCE can only be implemented by couple specimens with neighboring crack sizes.

3.3. Energy dissipation rate-based bond energy density criterion

For the elastic-plastic materials, as shown in Eq. (23), crack growth involves energy dissipation through the creation of new crack surfaces and additional global plastic energy. To overall capture ductile crack growth, the "energy dissipation rate" R was defined as [3,5]:

$$R = \frac{dW_s}{dA} + \frac{dU_p}{dA} \quad (26)$$

where dW_s/dA represents the crack surface separation energy dissipation rate, which is equal to surface fracture energy Γ_s . While dU_p/dA is called as the unrecoverable plastic energy rate, which means the non-recoverable mechanical energy during crack growth due to material plasticity. Most of plastic energy will be converted into heat related to the Taylor-Quinney coefficient [45].

In peridynamic ductile fracture modeling, cracks are formulated with directional broken bonds across crack surface. As the crack grows, the external potential energy is dissipated by the broken bonds for new crack surface, or transformed as plastic energy in global peridynamic points. Thus, the released energy of broken bonds is only related to the surface fracture energy Γ_s . Similar to the energy equivalence in [40], the total broken bond released energy at unit area of crack is equal to the surface fracture energy Γ_s , the critical bond energy density for the elastic-plastic fracture is obtained:

$$w_c = \begin{cases} \frac{4\Gamma_s}{\pi\delta^4} & 3D \\ \frac{3\Gamma_s}{2\delta^3 B} & 2D \end{cases} \quad (27)$$

where B is the thickness of the 2D model.

Then, the energy dissipation rate-based bond failure criterion can be expressed as:

$$\underline{d}(\xi) = \begin{cases} 1 & \text{if } \underline{w}^e(\xi) + \underline{w}^p(\xi) < w_c \text{ for all } t' \leq t, \\ 0 & \text{otherwise} \end{cases} \quad (28)$$

where $\underline{d} = 0$ means that the bond is irreversibly broken. The bond energy density is computed by the sum of elastic and plastic bond energy density in Eqs. (20) and (21).

The modified critical bond energy density for the elastic-plastic fracture is given in Eq. (28). Unlike the previous bond energy density criterion in [40], the surface fracture energy Γ_s , rather than critical energy release rate G_c , is used for the critical bond energy density computation. By using this energy dissipation rate-based bond failure criterion, the dissipation energy during crack growth can be quantitatively modeled as two decomposed parts: the broken bonds released energy from emerging crack surfaces and the plastic energy of global peridynamic points. Meanwhile, for the elastic brittle materials, the energy dissipation rate R is equal to energy release rate G , the critical energy release rate G_c is equal to surface fracture energy Γ_s , and the present bond failure criterion in Eq. (28) can be reduced into the origin version [40].

4. Numerical implementation

In peridynamic numerical model, the whole body is discretized into finite nodes, and the motion equation of the peridynamic point \mathbf{x}_i in Eq. (1) can be rewritten as:

$$\rho_i \ddot{\mathbf{u}}_i(\mathbf{x}_i, t) = \sum_{j \in H_i} \left\{ \underline{\mathbf{T}}[\mathbf{x}_i, t] \langle \mathbf{x}_j - \mathbf{x}_i \rangle - \underline{\mathbf{T}}[\mathbf{x}_j, t] \langle \mathbf{x}_i - \mathbf{x}_j \rangle \right\} V_j + \mathbf{b}_i(\mathbf{x}_i, t) \quad (29)$$

where i and j are the node numbers, and V_j is the volume of node j . The neighbor nodes j of the node i , satisfying $|\mathbf{x}_j - \mathbf{x}_i| \leq \delta$ are summed, where δ is the horizon size. With the uniform discrete grid size Δx , the horizon size can be expressed as $\delta = m\Delta x$. For the time iteration analysis, the explicit time integration scheme is utilized to obtain the final numerical solution. And the artificial damping would be added for the quasi-static problem analysis.

4.1. Elastic and plastic deformation states updating

In the time iterative process, the bond extension states for the next step need to be solved with the bond information of current step, based on the yield function and plastic flow rule.

At n step of time t_n , giving known bond extension states $\left\{ \underline{e}_n, \underline{e}_n^{dp} \right\}$, and the equivalent plastic strain ϵ_n^p of each peridynamic point. For $n+1$ step of time $t_{n+1} = t_n + \Delta t$, with the known \underline{e}_{n+1} , the unknown \underline{e}_{n+1}^{dp} and ϵ_{n+1}^p need to be computed using the yield function and plastic flow rule with the following steps:

- 1 First, give the trial elastic deviatoric extension state with zero plastic increment:

$$\underline{e}_{trial}^{de} = \underline{e}_{n+1} - \underline{e}_{n+1}^i - \underline{e}_n^{dp}, \Delta \underline{e}_{n+1}^{dp} = 0, \Delta \epsilon_{n+1}^p = 0 \quad (30)$$

- 2 Input the trial state into the yield function of Eq. (14):

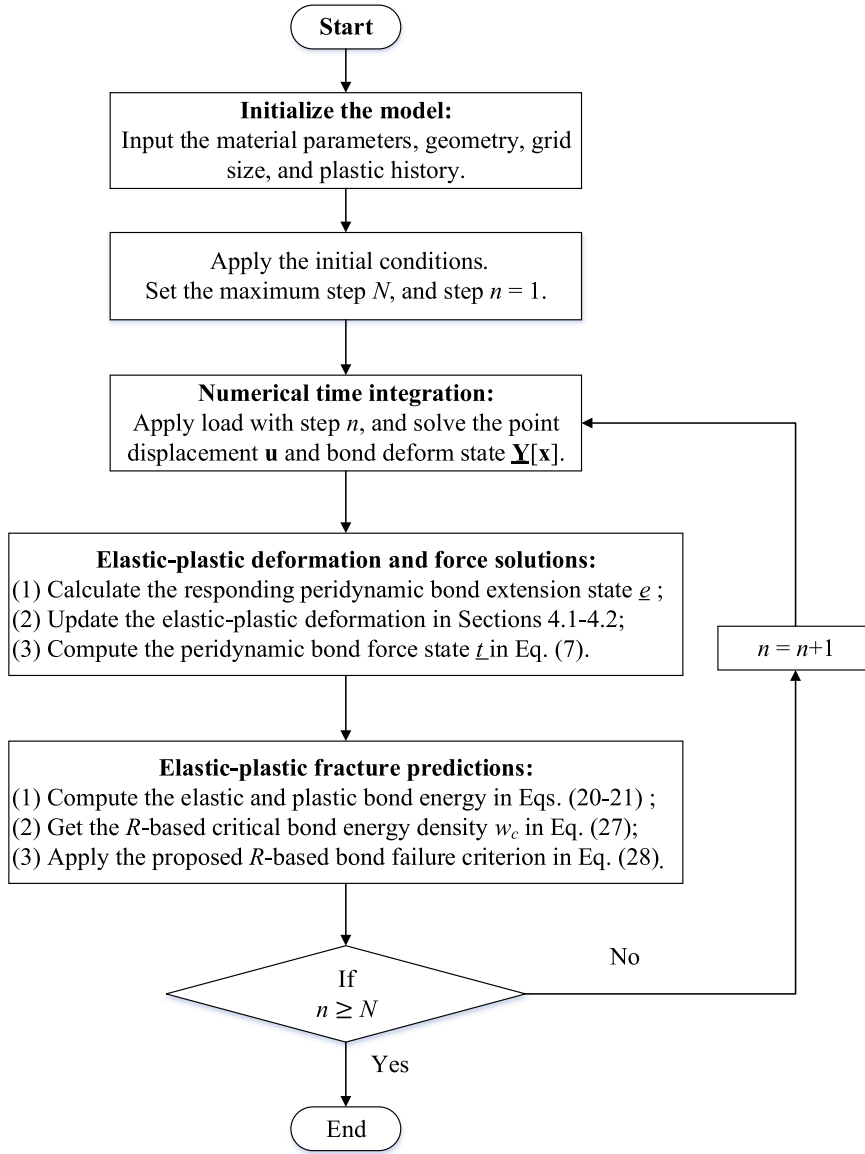


Fig. 3. The whole progress of elastic-plastic fracture analysis in peridynamics.

$$f_{trial} = W^d \left(\underline{\epsilon}_{trial}^{de} \right) - \psi \left(\epsilon_n^p \right) \quad (31)$$

where distortional strain energy density W^d is calculated with $\underline{\epsilon}_{trial}^{de}$ in Eq. (13), and hardening variable ψ is computed with ϵ_n^p .

3 For each peridynamic point, check whether the trial state is correct:

a) if $f_{trial} \leq 0$, the trial state is correct, and no new plastic increment occurs:

$$\underline{\epsilon}_{n+1}^{de} = \underline{\epsilon}_{trial}^{de}, \underline{\epsilon}_{n+1}^{dp} = \underline{\epsilon}_n^{dp}, \epsilon_{n+1}^p = \epsilon_n^p \quad (32)$$

b) if $f_{trial} > 0$, the trial state is not correct, and new plastic increment occurs. Based on the plastic flow rule in Eq. (17), the bond extension states should obey:

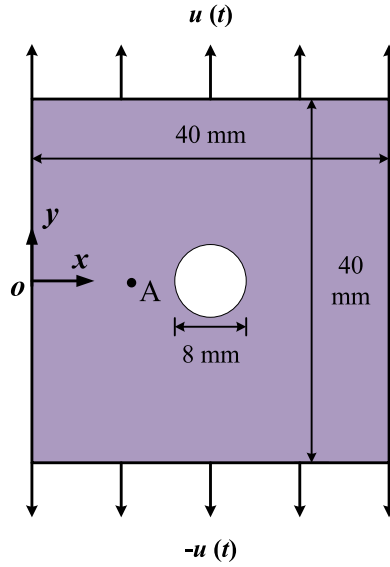


Fig. 4. The elastic-plastic plate with a central hole under displacement loading.

Table 1

Material parameters for the elastic-plastic plate.

	Elastic modulus E (GPa)	Poisson's ratio ν	Density ρ (kg/m ³)	Yield stress σ_Y (GPa)	Hardening modulus H (GPa)
Material	100	0.342	4428	1.0	20

$$\Delta \underline{\epsilon}_{n+1}^{dp} = \lambda \alpha \omega \underline{\epsilon}_{n+1}^{de}, \underline{\epsilon}_{n+1}^{de} = \underline{\epsilon}_{n+1}^{de} - \Delta \underline{\epsilon}_{n+1}^{dp} \tag{33}$$

Considering the known $\underline{\epsilon}_{n+1}^{de} = \underline{\epsilon}_{n+1} - \underline{\epsilon}_{n+1}^i - \underline{\epsilon}_n^{dp}$, Eq. (33) can be rewritten as:

$$\Delta \underline{\epsilon}_{n+1}^{dp} = \frac{\lambda \alpha \omega \underline{\epsilon}_{n+1}^{de}}{1 + \lambda \alpha \omega}, \underline{\epsilon}_{n+1}^{de} = \frac{\underline{\epsilon}_{n+1}^{de}}{1 + \lambda \alpha \omega} \tag{34}$$

where α is the peridynamic constant in Eq. (6), the undetermined parameter λ can be resolved by the yield function of $f(\underline{\epsilon}_{n+1}^{de}, \epsilon_{n+1}^p) = 0$, which will be specifically given in the following section. Submit $\Delta \underline{\epsilon}_{n+1}^{dp}$ into Eq. (19), increment equivalent plastic strain $\Delta \epsilon_{n+1}^p$ can be obtained, and $\epsilon_{n+1}^p = \epsilon_n^p + \Delta \epsilon_{n+1}^p$.

4.2. Solution of yield function for the parameter λ

In this section, the undetermined parameter λ in the plastic flow rule is resolved based on the yield function of $f(\underline{\epsilon}_{n+1}^{de}, \epsilon_{n+1}^p) = 0$, for the 3D and 2D cases.

First, considering the bond extension states at $n + 1$ step, the distortional strain energy density in Eq. (13) can be rewritten into:

$$W_{n+1}^d = \frac{1}{2} k^d (\theta_{n+1})^2 + \frac{\alpha}{2} \left(\omega \underline{\epsilon}_{n+1}^{de} \right) \cdot \underline{\epsilon}_{n+1}^{de} \tag{35}$$

where the volume dilatation θ_{n+1} is computed in Eq. (4) with the known $\underline{\epsilon}_{n+1}$, and the peridynamic constants k^d and α are:

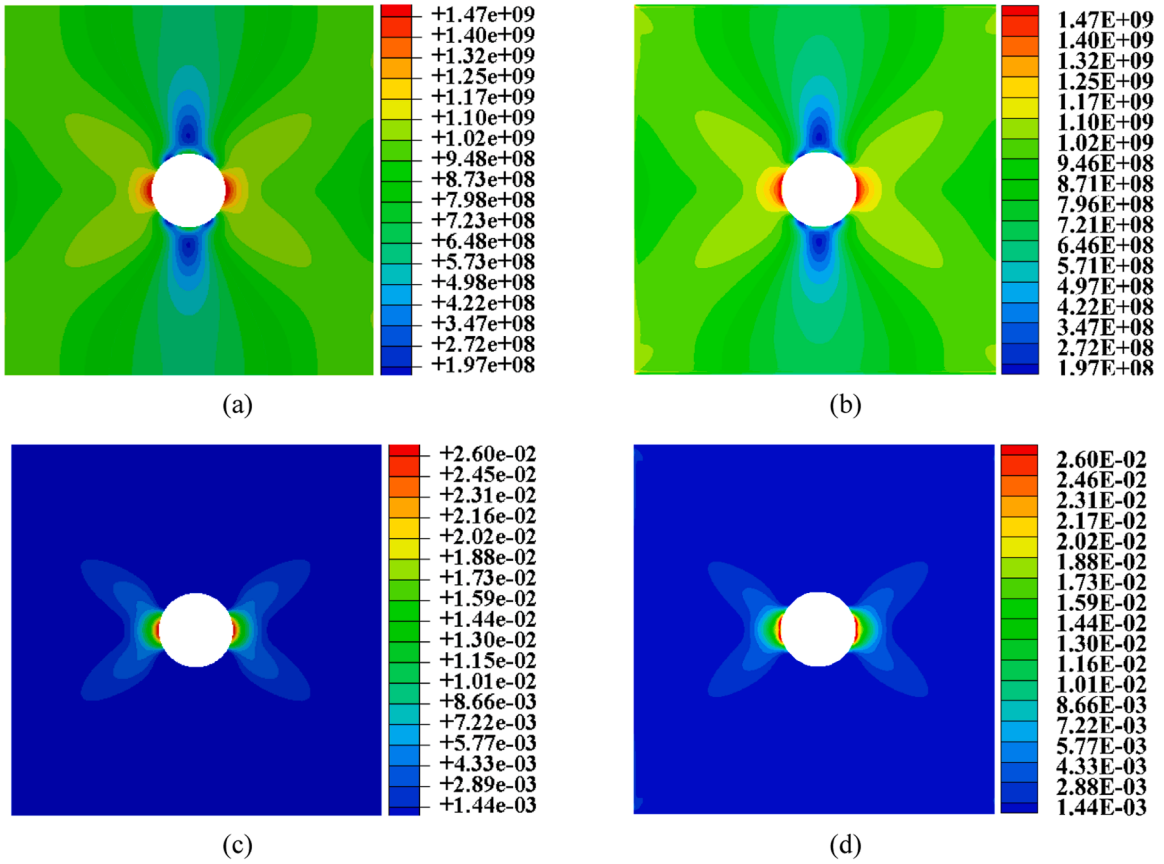


Fig. 5. Comparisons of equivalent Mises stress: (a) FEM and (b) Peridynamics, and equivalent plastic strain: (c) FEM and (d) peridynamics with displacement load of $u = 0.2$ mm in the plane stress case.

$$\begin{cases} k^d = 0, \alpha = \frac{15\mu}{q} & \text{3D} \\ k^d = \frac{E(1+\nu)}{6(1-\nu)^2}, \alpha = \frac{8\mu}{q} & \text{Plane stress} \\ k^d = \frac{E}{6(1+\nu)}, \alpha = \frac{8\mu}{q} & \text{Plane strain} \end{cases} \quad (36)$$

Substitute the bond extension states of Eq. (34) into Eq. (35), the Eq. (35) can then be expressed as:

$$W_{n+1}^d = \frac{1}{2}k^d(\theta_{n+1})^2 + \frac{\alpha}{2(1+\lambda\alpha)^2} \left(\underline{\epsilon}_{trial}^{de} \right) \cdot \underline{\epsilon}_{trial}^{de} \quad (37)$$

where the constant influence function $\underline{\omega} = 1$ is considered for equation simplification.

For the linear isotropic strain hardening materials, the hardening variable at $n + 1$ step is

$$\psi_{n+1} = \frac{(\sigma_Y + H\epsilon_{n+1}^p)^2}{6\mu} \quad (38)$$

where $\epsilon_{n+1}^p = \epsilon_n^p + \Delta\epsilon_{n+1}^p$, Input $\Delta\epsilon_{n+1}^{dp}$ in Eq. (34) into Eq. (19), the increment equivalent plastic strain $\Delta\epsilon_{n+1}^p$ is obtained:

$$\Delta\epsilon_{n+1}^p = \begin{cases} \frac{\lambda\alpha}{1+\lambda\alpha} \sqrt{\frac{5}{q} \left(\underline{\epsilon}_{trial}^{de} \right) \cdot \underline{\epsilon}_{trial}^{de}} & \text{3D} \\ \frac{\lambda\alpha}{1+\lambda\alpha} \sqrt{\frac{2}{q} \left(\underline{\epsilon}_{trial}^{de} \right) \cdot \underline{\epsilon}_{trial}^{de}} & \text{2D} \end{cases} \quad (39)$$

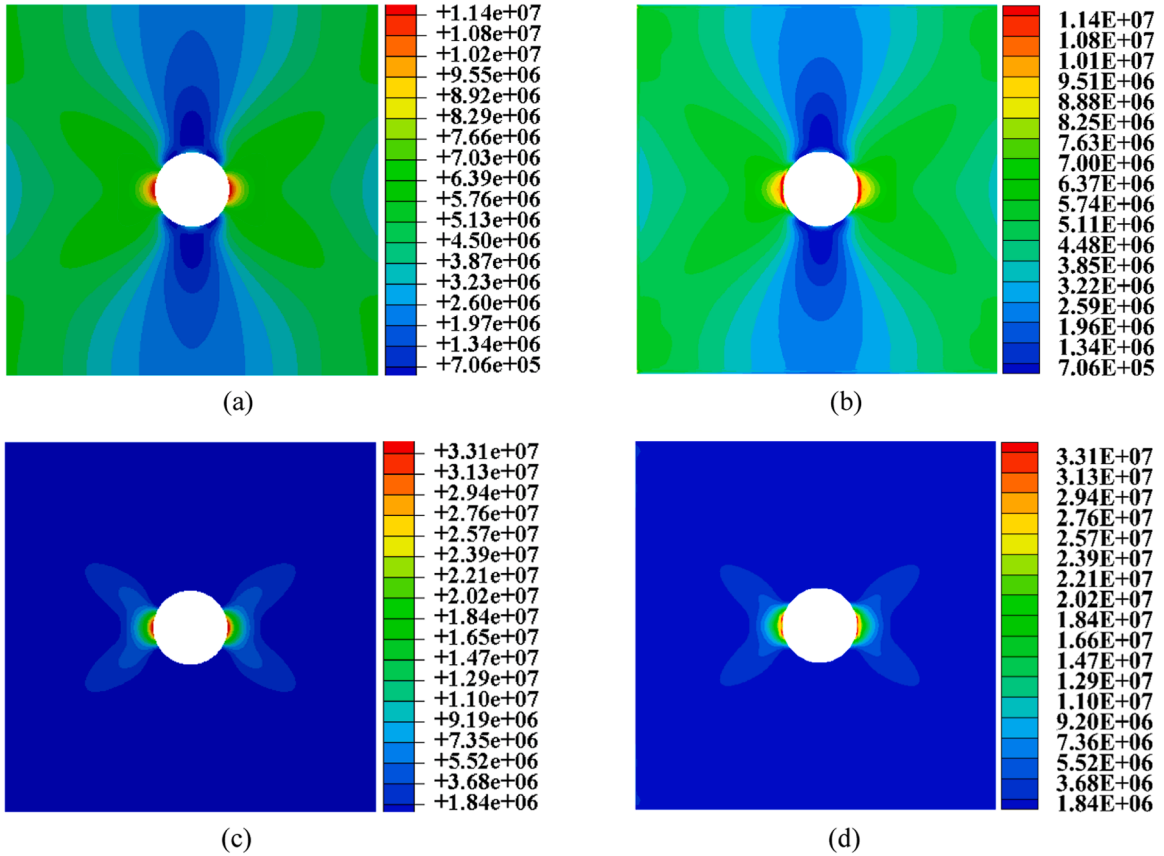


Fig. 6. Comparisons of elastic strain energy density: (a) FEM and (b) Peridynamics, and plastic strain energy density: (c) FEM and (d) peridynamics with load of $u = 0.2$ mm in the plane stress case.

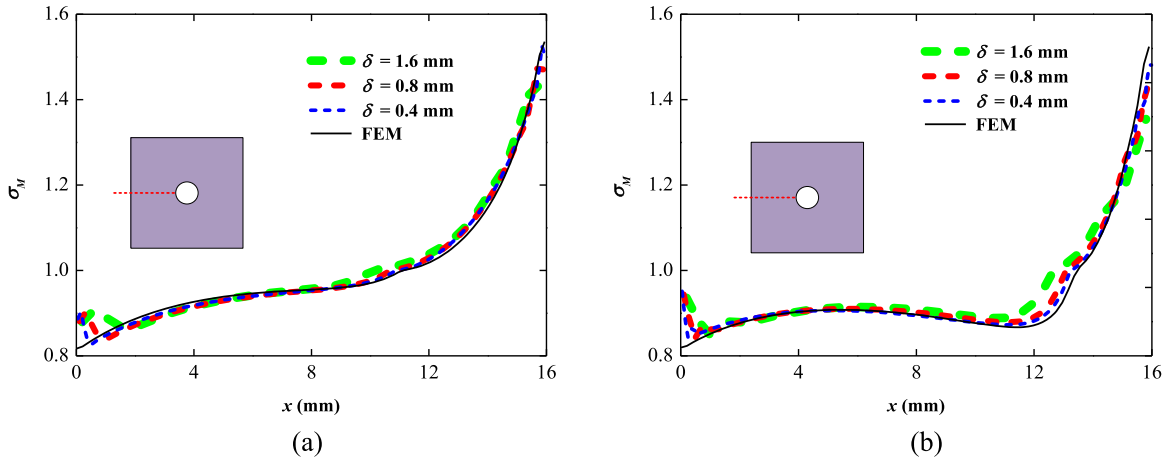


Fig. 7. The equivalent Mises stress along the x -axis with different values of δ in the plane stress (a) and plane strain (b) cases.

Substitute the Eqs. (37) and (38) into $W_{n+1}^d - \psi_{n+1} = 0$, the yield function can be expressed as:

$$\frac{1}{2}k^d(\theta_{n+1})^2 + \frac{\alpha}{2(1 + \lambda\alpha)^2} \left(\frac{e_{trial}^{de}}{z_{trial}} \right) \cdot e_{trial}^{de} - \frac{\{\sigma_0 + H(\epsilon_n^p + \Delta\epsilon_{n+1}^p(\lambda))\}^2}{6\mu} = 0 \tag{40}$$

where $\Delta\epsilon_{n+1}^p(\lambda)$ is the function of λ that given in Eq. (39). In this form of yield function, only parameter λ is unknown. The Eq. (40) can

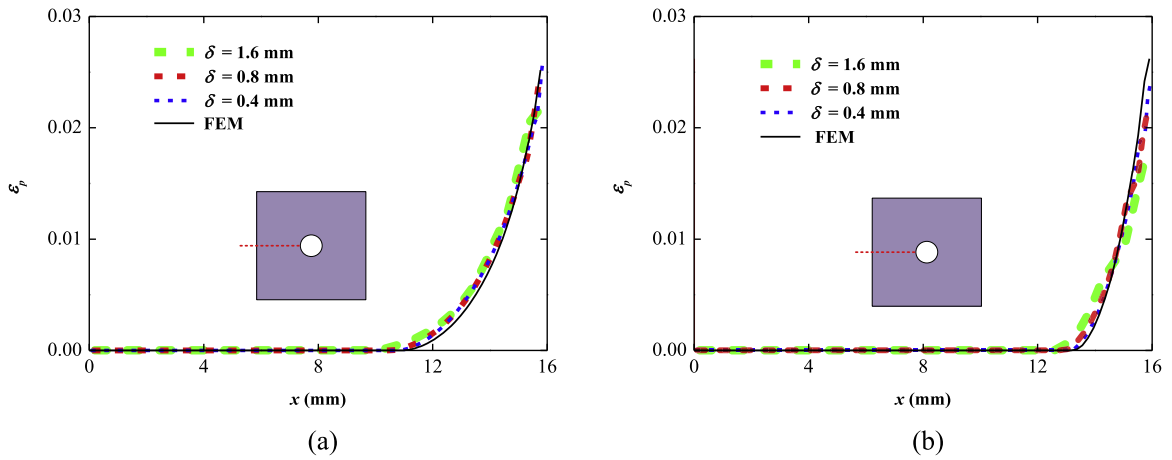


Fig. 8. The equivalent plastic strain along the x-axis with different values of δ in the plane stress (a) and plane strain (b) cases.

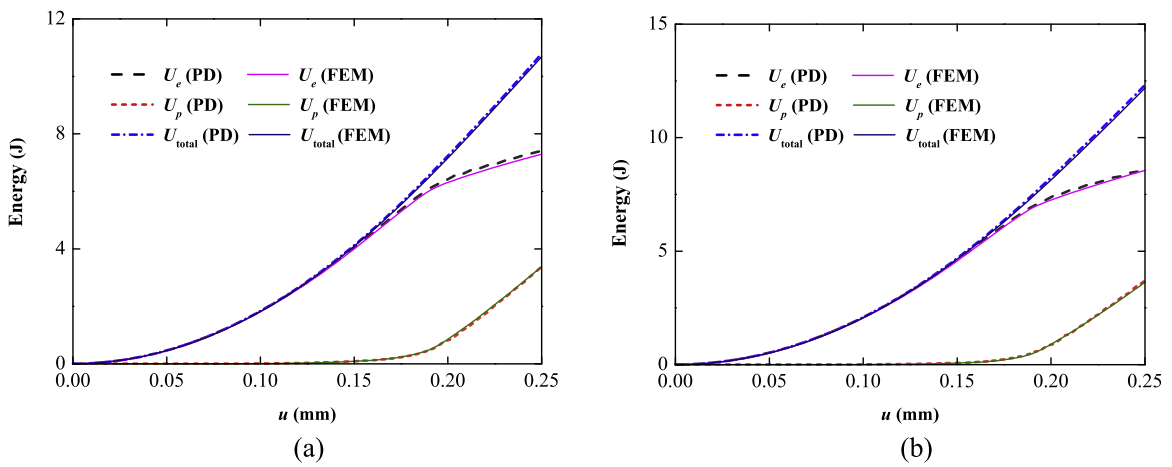


Fig. 9. The elastic strain energy (U_e), plastic strain energy (U_p) and total strain energy (U_{total}) of the plate with increasing displacement load in the plane stress (a) and plane strain (b) cases.

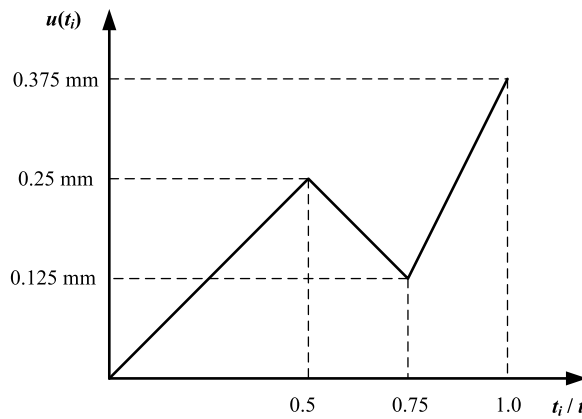


Fig. 10. The changing displacement load for the loading, unloading and reloading processes.

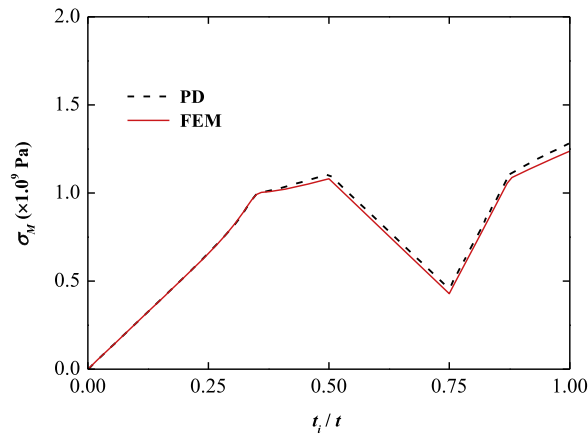


Fig. 11. The equivalent Mises stress of point A during the loading, unloading and reloading processes.

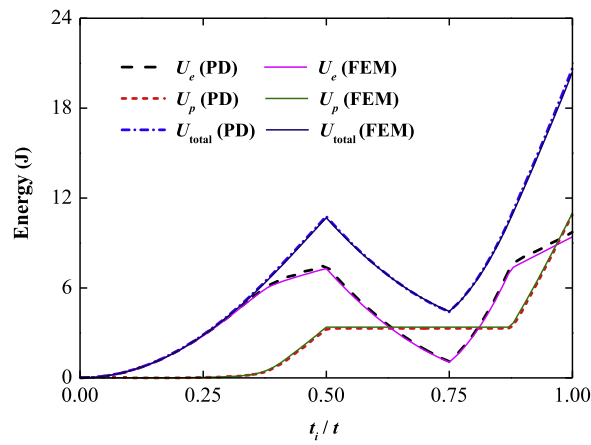


Fig. 12. The elastic strain energy (U_e), plastic strain energy (U_p) and total strain energy (U_{total}) of the plate during the loading, unloading and reloading processes.

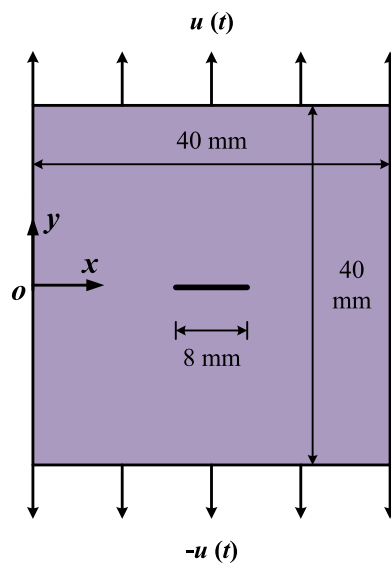


Fig. 13. The elastic-plastic plate with a central crack under displacement loading.

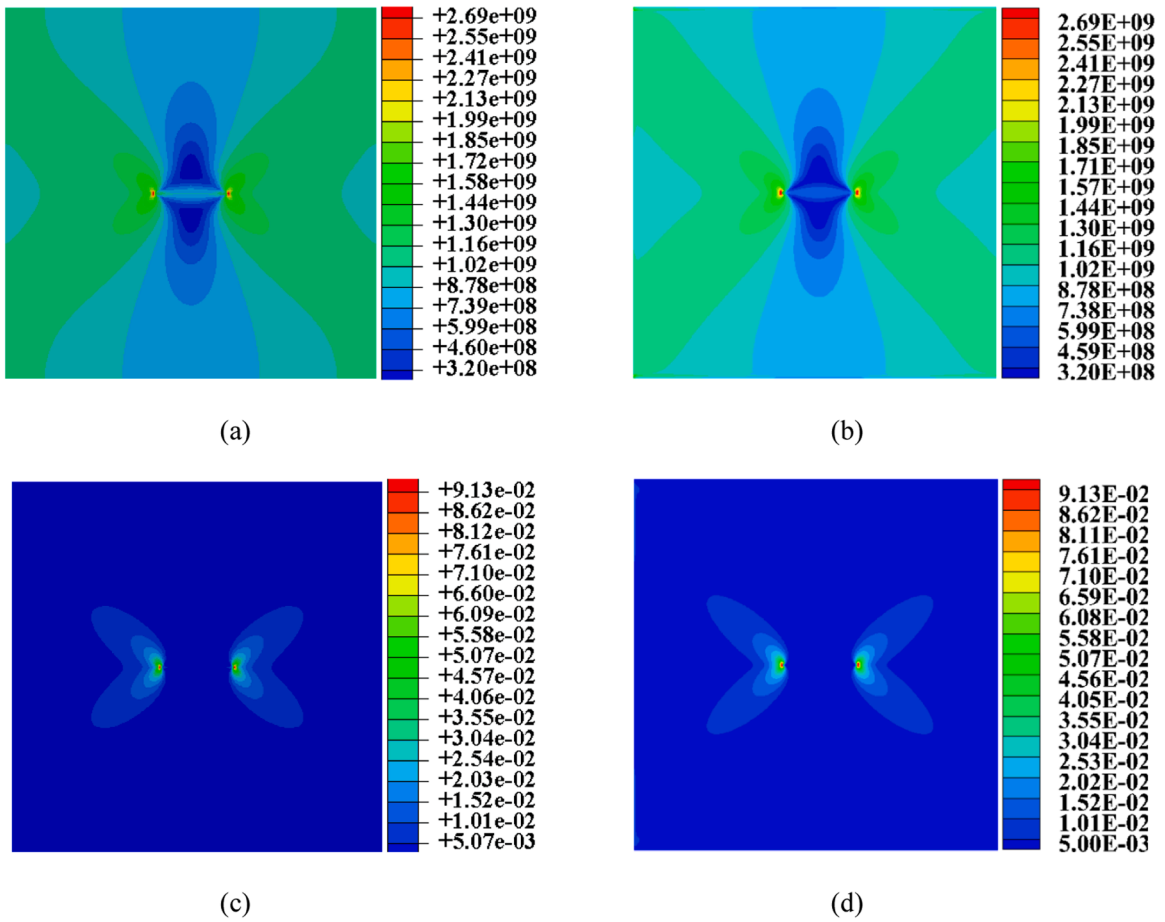


Fig. 14. Comparisons of equivalent Mises stress: (a) FEM and (b) Peridynamics, and equivalent plastic strain: (c) FEM and (d) peridynamics with displacement load of $u = 0.25$ mm in plane stress case.

be transformed into the quadratic equation of λ , which can be easily resolved.

Thus, unlike the previous peridynamic elastic-plastic models in [24,31], for the linear hardening materials, the yield function can be directly solved in present model by Eq. (40) both for the 3D and 2D cases, no iterative process is required. That is because the present yield function of Eq. (14) and plastic flow rule of Eq. (17) are both defined only with the bond elastic deviatoric extension e^{de} , no bond force state is related. The unknown λ is decomposed from the dot product, and the yield function can be transformed into the quadratic equation of parameter λ . However, if the material hardening law is nonlinear, the iterative process is still needed for the nonlinear function solution.

4.3. Process of elastic-plastic fracture in peridynamics

The process of peridynamics-based frame for elastic-plastic ductile fracture is given in Fig. 3.

As shown in Fig. 3, for the elastic-plastic material modeling, the trial check method in Section 4.1 is utilized to update the elastic and plastic deformation states, and the yield function can be resolved in Section 4.2. The peridynamic bond force state can be obtained in Eq. (7) with the updated elastic deviatoric extension. For the elastic-plastic fracture analysis, the energy dissipation rate-based bond energy density criterion is applied, in which elastic and plastic bond density energy are calculated in Eqs. (20) and (21), and the critical value is computed in Eq. (27).

In summary, a peridynamics-based frame is established for elastic-plastic fracture analysis. It can be utilized for elastic-plastic deformation analysis, and also elastic-plastic crack growth prediction.

5. Numerical examples

In this section, three numerical examples are studied. The elastic-plastic plates with a center hole or a center crack are analyzed for the proposed peridynamic elastic-plastic model verifications. Then, an elastic-plastic fracture example, the compact tension (CT) test, is quantitatively investigated for ductile crack growth study.

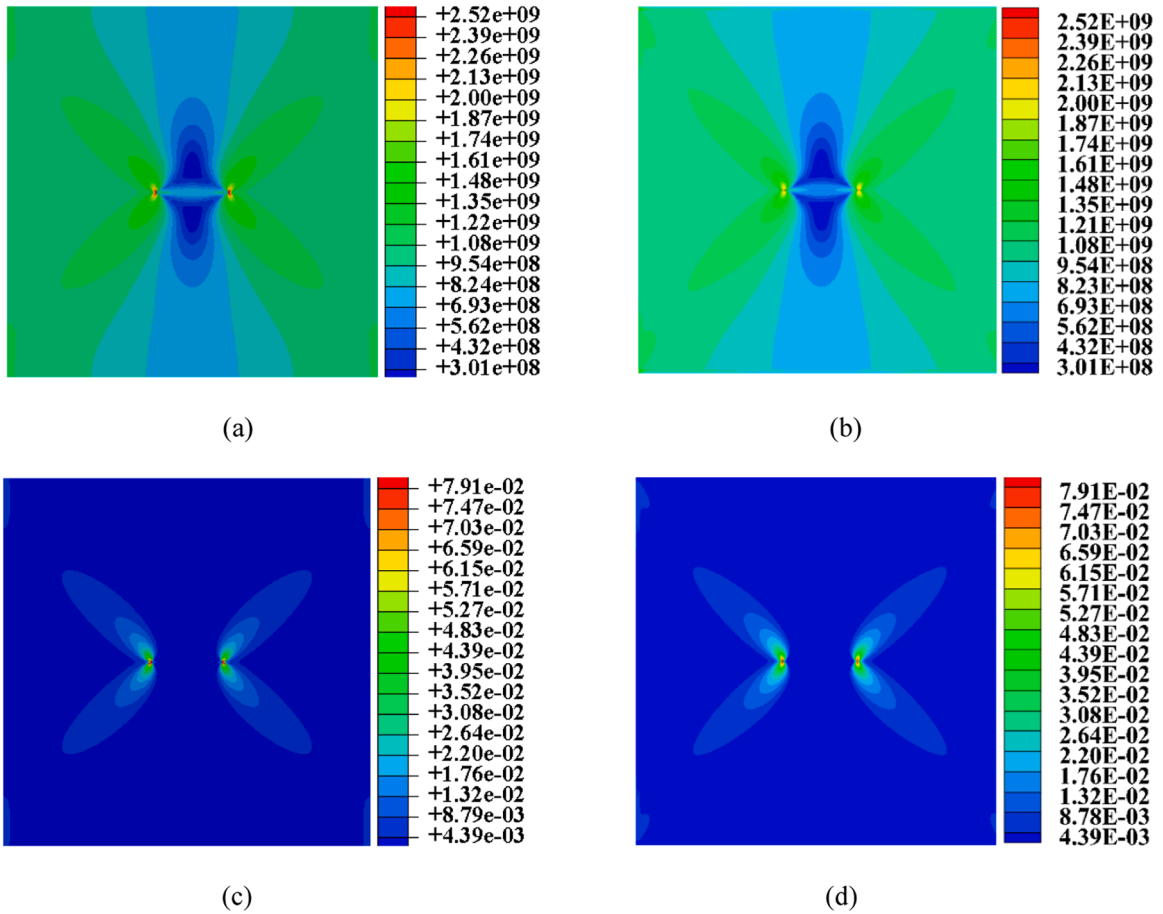


Fig. 15. Comparisons of equivalent Mises stress: (a) FEM and (b) Peridynamics, and equivalent plastic strain: (c) FEM and (d) peridynamics with displacement load of $u = 0.25$ mm in plane strain case.

5.1. An elastic-plastic plate with a center hole

A plate with a central open hole under displacement loading is first considered to validate the proposed peridynamic model for elastic-plastic deformation analysis. The geometrical sizes of the plate are shown in Fig. 4, and plane stress and plane strain conditions are, respectively considered, the plate thickness B is 1 mm. The elastic-plastic material with linear isotropic strain hardening is considered, and material properties are given in Table 1.

In the numerical peridynamic model, uniform mesh size is utilized. The peridynamic elastic-plastic model is utilized for elastic-plastic behaviors prediction of this open-holed plate, and the adaptive dynamic relaxation (ADR) method [46] is utilized for quasi-static analysis. The results predicted by peridynamics are compared with those from the numerical finite element method (FEM), and the relative difference of peridynamic result to FEM solution is computed.

For nonlocal peridynamic theory, the material points near boundary do not have a full horizon, which leads to the surface effect [47]. Since the skin effect can be relieved with the refined mesh sizes, the mesh refinement method [48] is utilized to handle this skin effect for simplification. Moreover, the surface correction [47,49] or the PD differential operator based methods [50] are other effective strategies to solve the skin effect.

5.1.1. Elastic-plastic behaviors of open-holed plate

First, the fixed displacement load of $u = 0.2$ mm is applied on the plate boundaries (see Fig. 4). The plots of equivalent Mises stress and equivalent plastic strain of the plate from the present peridynamic model and the FEM are given in Fig. 5; while distributions of elastic and plastic strain energy density are presented in Fig. 6, where the fixed values of $\delta = 0.4$ mm and $m = 4$ with the plane stress condition are utilized. As shown in Figs. 5-6, the equivalent Mises stress, equivalent plastic strain, elastic and plastic strain energy density from the present model all greatly match those from the FEM solutions.

For quantitative comparison, the equivalent Mises stress and equivalent plastic strain along the x-axis are presented in Figs. 7 and 8, where horizon values of $\delta = 1.6$ mm, 0.8 mm and 0.4 mm, and a fixed value of $m = 4$ are considered for the δ -convergence [51]. Generally, it is shown that the results by proposed peridynamic elastic-plastic model are converging to the FEM solution as nonlocal

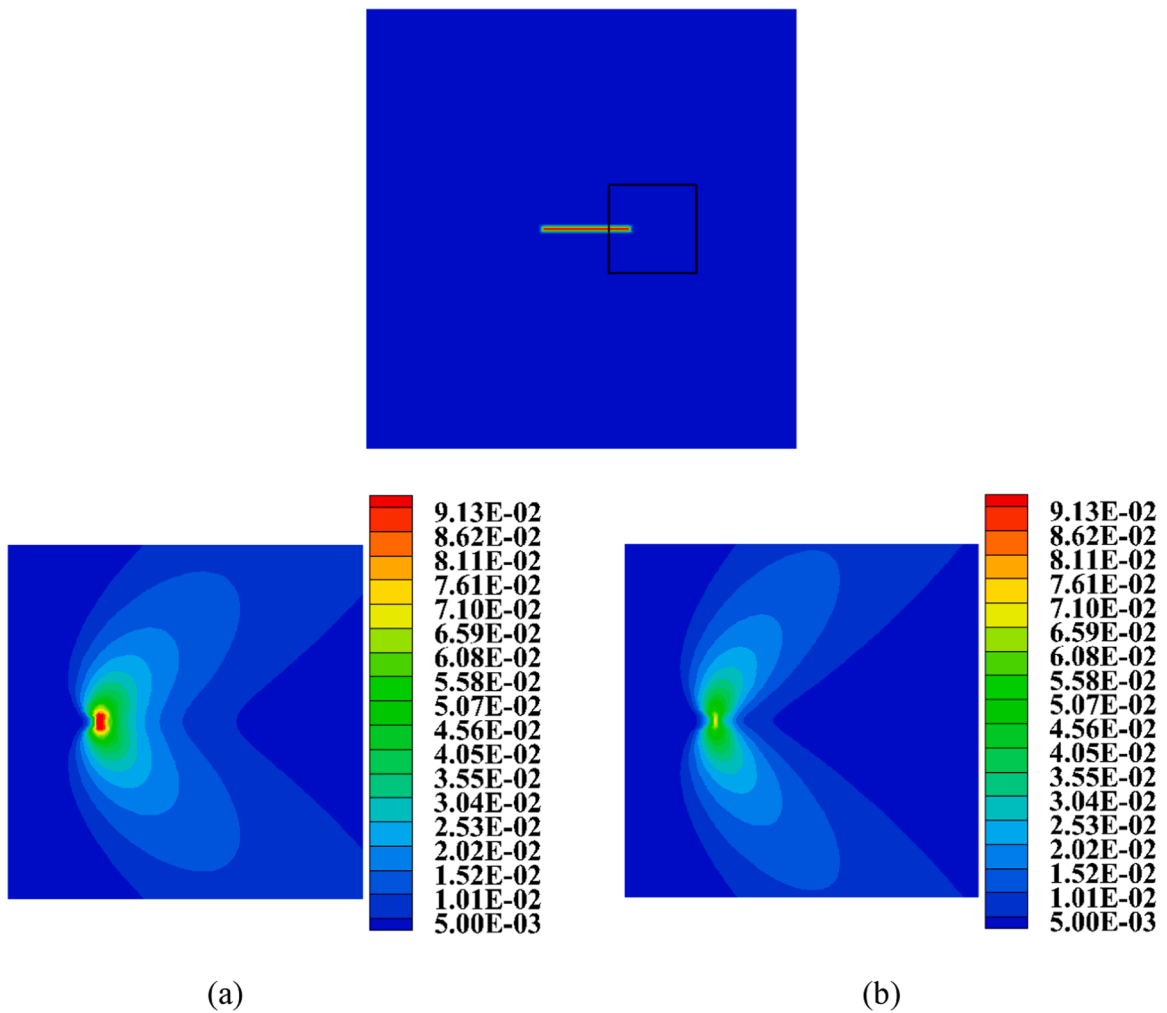


Fig. 16. Distributions of equivalent plastic strain zoom-in at the crack tip in the (a) plane stress and (b) plane strain cases.

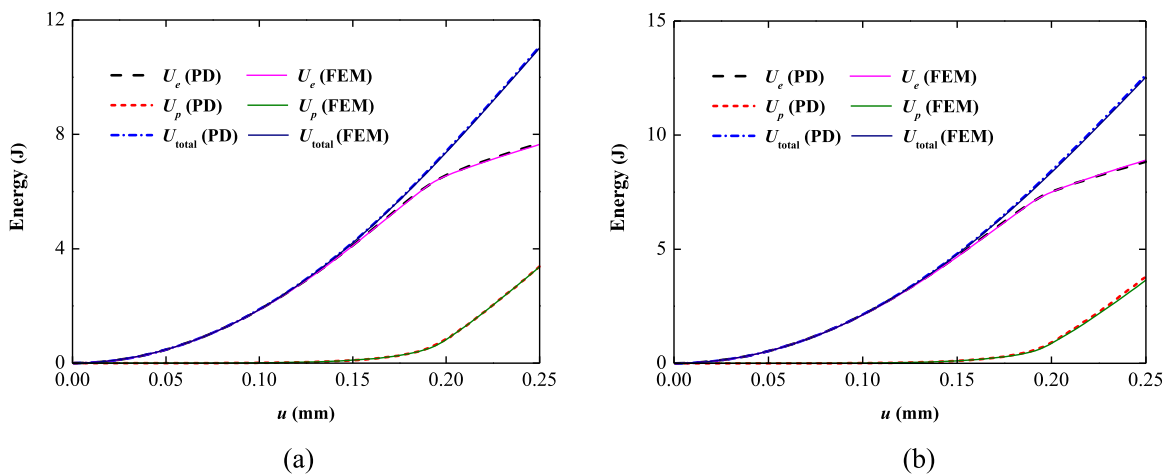


Fig. 17. The elastic strain energy (U_e), plastic strain energy (U_p) and total strain energy (U_{total}) of the whole system with increasing displacement load in the plane stress (a) and plane strain (b) cases.

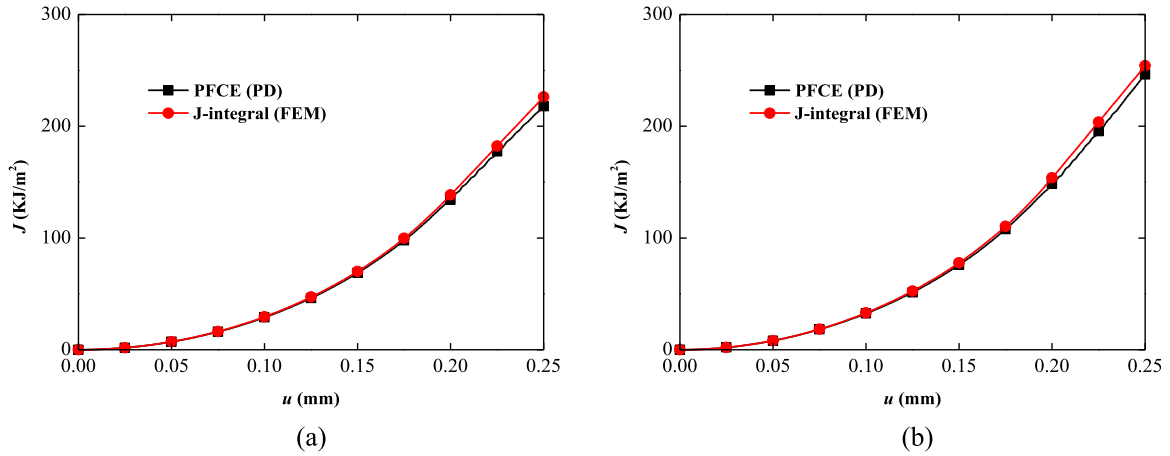


Fig. 18. The nonlinear energy release rate (J) of the center crack with increasing displacement load in the plane stress (a) and plane strain (b) cases.

horizon δ decreases, in both plane stress and plane strain cases. While the equivalent Mises stress of points within δ values of distance to the boundary are not reliable because of the nonlocal surface effect [47]. However, this skin effect can be relieved with the refining mesh sizes, and it has no much effect on points away from the boundary (see Fig. 7).

Additionally, curves of the elastic strain energy, plastic strain energy and total strain energy of the plate under the linearly increasing displacement are given in Fig. 9. As shown, both for plane stress and plane strain cases, the strain energy density values predicted by peridynamics greatly fit the FEM solutions with the maximum relative difference of 2.0 %.

5.1.2. Loading and unloading behaviors

Then, the changing displacement load $u(t_i)$ in Fig. 10 is applied on the plate for loading, unloading and reloading processes. The point A (15 mm, 0 mm) near the open-hole edge (see Fig. 4) is typically analyzed, and the plane stress condition is considered. The adaptive dynamic relaxation (ADR) method [46] is used for each step quasi-static analysis.

The equivalent Mises stress of point A during the loading, unloading and loading processes is presented in Fig. 11. As presented, in first loading process, the equivalent Mises stress curve increases with displacement load, and then bends around $u = 0.18$ mm for a smaller growth slope since the material point A yields and material hardening happens; when decreasing displacement is applied at the middle step, the curve linearly decreases for the material elastic unloading. In the last reloading process, the stress curve firstly elastically increases and bends at $u = 0.245$ mm when the material point A yields again. Meanwhile, the elastic strain energy, plastic strain energy and total strain energy of the plate during the loading, unloading and reloading processes are plotted in Fig. 12. Typically, the plastic strain energy is changeless during $t_i / t = 0.50$ – 0.87 for the elastic unloading and reloading processes. The stress and the energy curves predicted from the peridynamics are greatly consistent to the FEM results within the relative difference of 3.8 %.

5.2. An elastic-plastic plate with a center crack

A plate with a center crack is then analyzed. The geometrical sizes and loading conditions are presented in Fig. 13. The fixed thickness is 1 mm, and plane stress and plane strain conditions are all considered. The elastic-plastic material in Table 1 is still utilized. For the peridynamic modeling, uniform mesh size is used. The elastic-plastic behaviors of this notched plated are predicted by peridynamics and compared with those from the FEM solutions.

5.2.1. Elastic-plastic behaviors of the plate with a central crack

The plots of equivalent Mises stress and equivalent plastic strain in plane stress and plane strain cases are, respectively presented in Figs 14–15, where the fixed displacement load of $u = 0.25$ mm is applied on the plate, and the fixed values of $\delta = 0.4$ mm and $m = 4$ are used. As shown, both for plane stress and plane strain cases, the equivalent Mises stress and equivalent plastic strain obtained by the proposed peridynamic elastic-plastic model closely match those from the FEM.

The equivalent plastic strain zoom-in at the crack tip is given in Fig. 16, which shows that the plastic strain value and size at the crack tip are much larger in plane stress than in plane strain. It is because the triaxial stress state associated with the plane strain condition restricts its plastic deformation, which is accordant with the analytical solution of the plastic size in [52].

Additionally, the elastic strain energy, plastic strain energy and total strain energy of the plate with increasing displacement are plotted in Fig. 17. As shown, the strain energy density results from peridynamics closely fit the FEM solutions both in plane stress and plane strain cases.

5.2.2. Nonlinear energy release rate

Then, the nonlinear energy release rate (J) is computed with the extended peridynamic finite crack extension (PFCE) method in Eq.

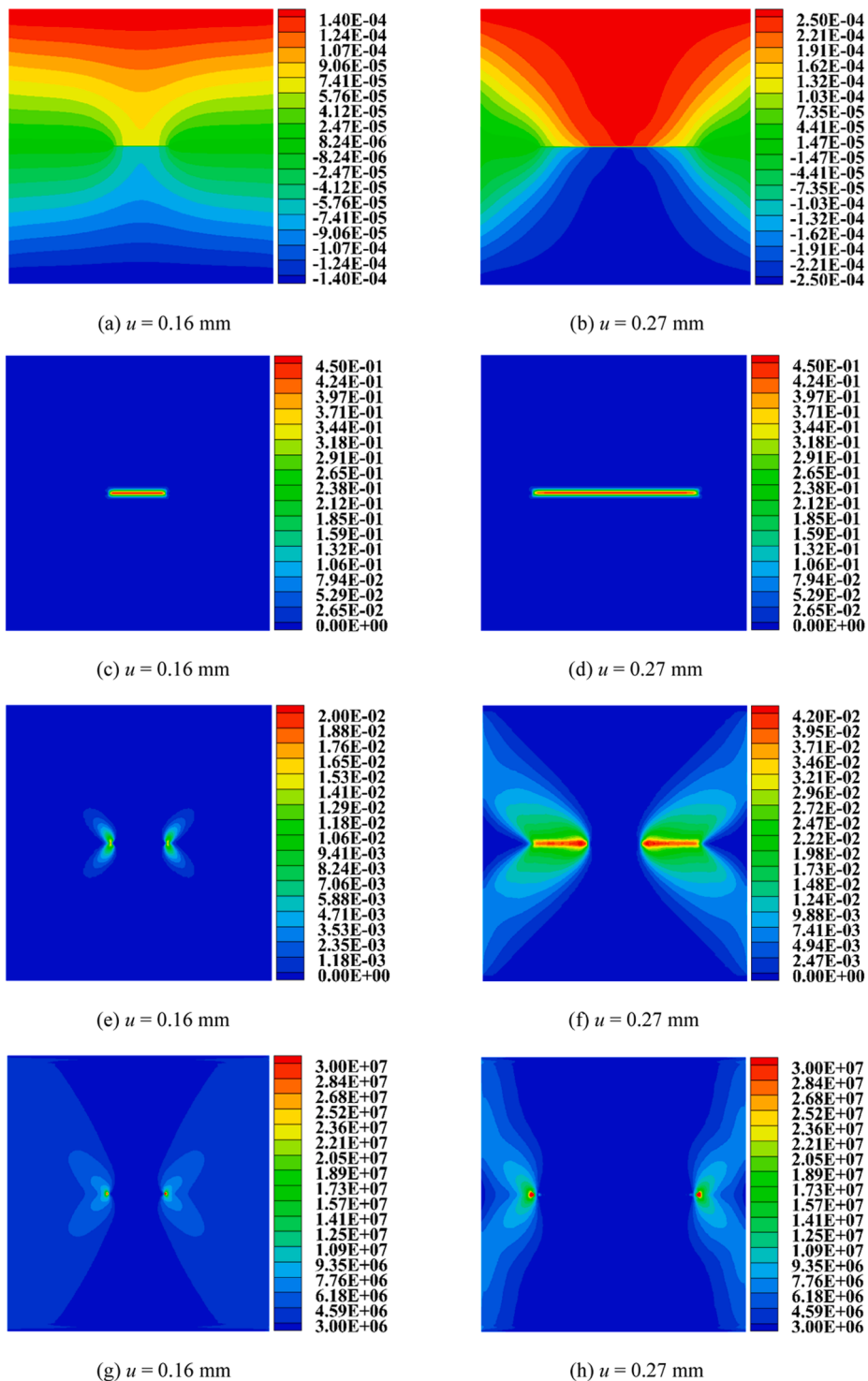


Fig. 19. Y-direction displacement (m) [(a) and (b)], local damage/crack path [(c) and (d)], equivalent plastic strain [(e) and (f)] and elastic strain energy density (J/m^3) [(g) and (h)] of center-notched plate with the typical displacement loads.

(25), and compared to the J-integral values from the numerical FEM solution. The increasing displacement loads from 0 mm to 0.25 mm are applied.

The curves of nonlinear energy release rate of the center crack with increasing displacement are presented in Fig. 18, where plane stress and plane strain cases are, respectively considered. As shown, the J values nonlinearly increase with the increasing displacement

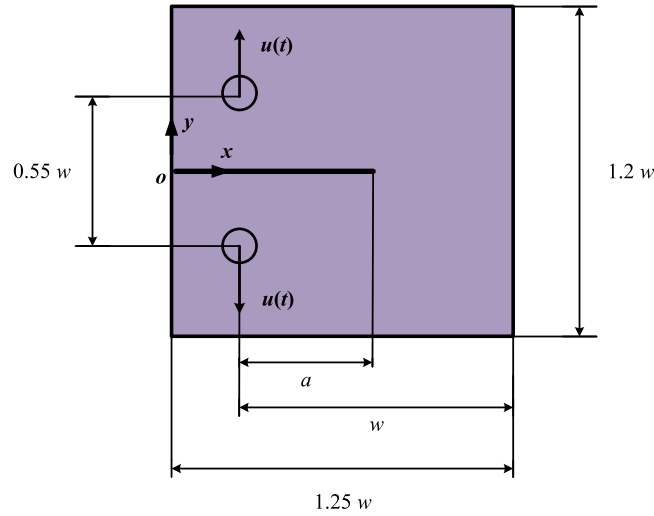


Fig. 20. The compact tension (CT) specimen.

Table 2

Material constants for the CT specimen.

	Elastic modulus E (GPa)	Poisson's ratio ν	Density ρ (kg/m ³)	Yield stress σ_Y (MPa)	Hardening modulus H (GPa)
Material	213	0.3	7850	443.1	3.45

load. The J values calculated from the extended PFCE method are consistent to those from the FEM J-integral within the relative difference of 3.9 %.

5.2.3. Ductile crack growth of center-notched plate

The ductile crack growth behaviors of center-notched plate are then predicted. The linear increasing displacement load is applied, and the plane strain condition is typically considered. The mesh sizes of $\delta = 0.8$ mm and $m = 4$ are used. For elastic-plastic fracture analysis, the energy dissipation rate-based bond failure criterion in Eq. (28) is utilized, and the surface fracture energy $\Gamma_s = 100$ KJ/m² is considered.

Distributions of y-direction displacement, crack path, equivalent plastic strain, and elastic strain energy density of the center-notched plate at typical displacement loads of $u = 0.16$ mm and 0.27 mm are presented in Fig. 19. As shown, with the increasing displacement load, the crack starts to grow from two pre-crack tips, and grows symmetrically along the pre-crack (see Figs. 19(c) and (d)). The equivalent plastic strain first appears around crack tips (see Fig. 19(e)), then distributes along the fresh crack surfaces and nearby large areas (see Fig. 19(f)). While the elastic strain energy density is first concentrated at two crack tips (see Fig. 19(g)), then moving with the crack tip (see Fig. 19(f)), which means unloading happens and the elastic energy releases after the crack tips pass by.

5.3. Compact tension (CT) test of elastic-plastic materials

The compact tension (CT) (see Fig. 20) is a common specimen for measurement of fracture toughness of metallic materials. Based on the ASTM standard of CT test [53], the nonlinear energy release rate or J-Integral value can be given in terms of its elastic and plastic components:

$$J = J_e + J_p = \frac{K^2(1 - \nu^2)}{E} + \frac{\eta U_p}{B(w - a)} \quad (41)$$

where:

$$K = \frac{P}{B\sqrt{w}} f(a/w), \eta = 2 + 0.522(1 - a/w) \quad (42)$$

and

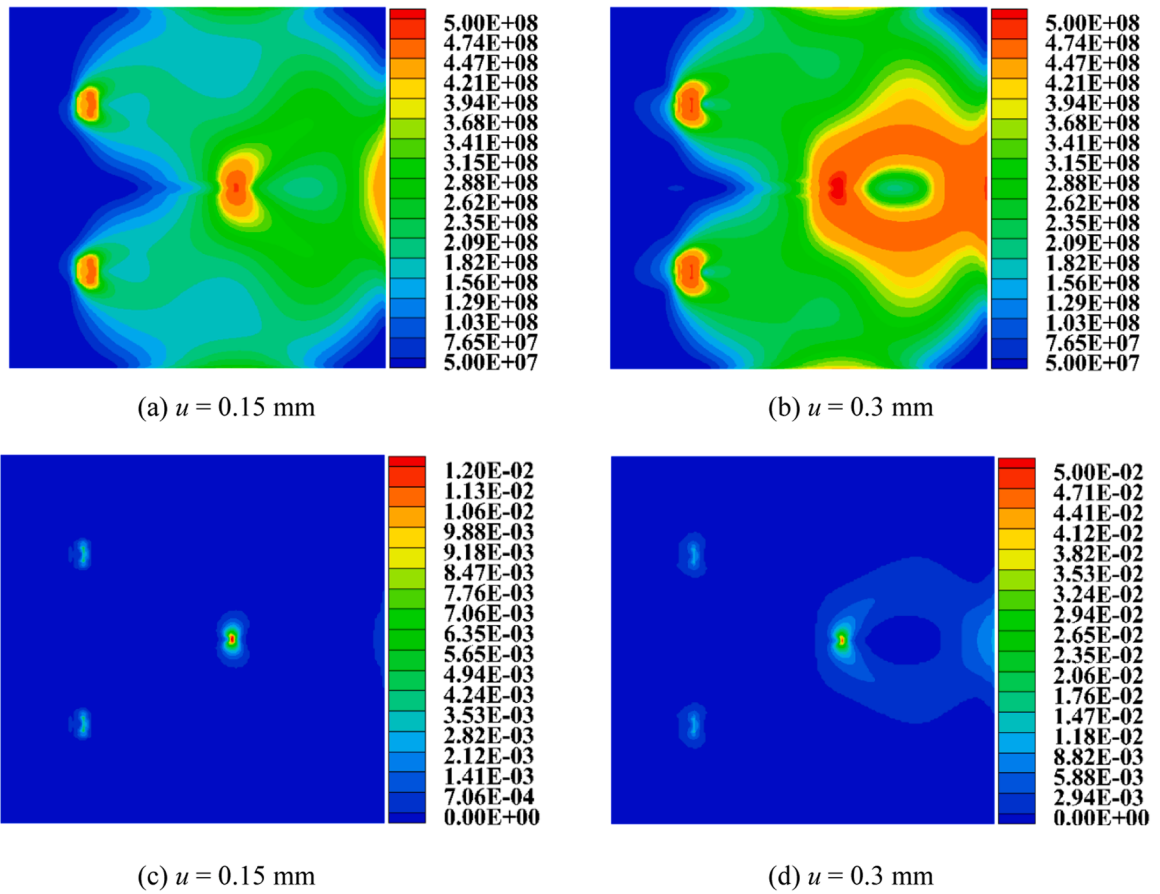


Fig. 21. Equivalent Mises stress [(a) and (b)] and equivalent plastic strain [(c) and (d)] of CT specimen with the typical displacement loads.

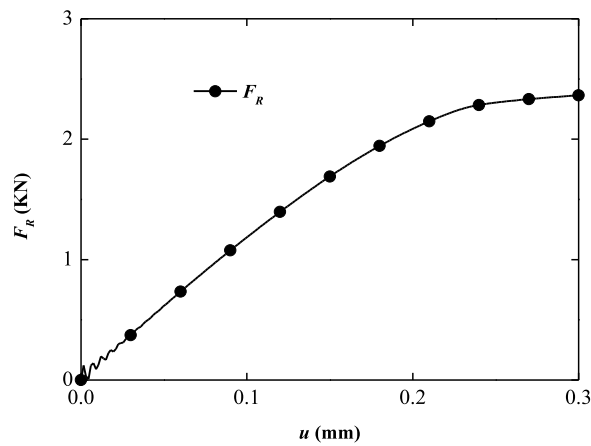


Fig. 22. Applied force versus displacement load during the CT test without crack growth.

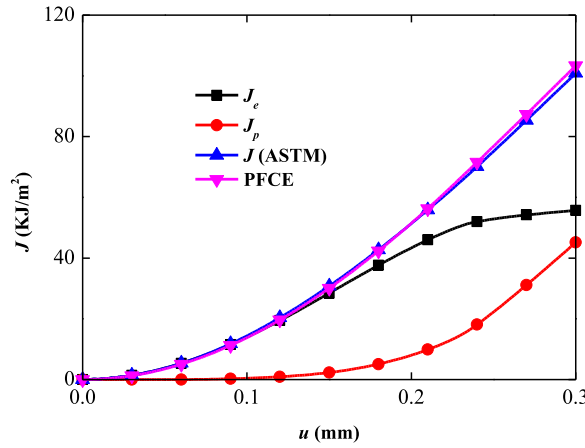


Fig. 23. The nonlinear energy release rate (J) computed by the ASTM equation, and the PFCE model with the increasing displacement loading.

$$f\left(\frac{a}{w}\right) = \frac{\left(2 + \frac{a}{w}\right) \left[0.886 + 4.46\frac{a}{w} - 13.32\left(\frac{a}{w}\right)^2 + 14.72\left(\frac{a}{w}\right)^3 - 5.6\left(\frac{a}{w}\right)^4\right]}{\left(1 - \frac{a}{w}\right)^{3/2}} \quad (43)$$

where K is the stress intensity factor, P is the applied load, U_p is the total plastic energy, a is the crack length, w is the width and B is the thickness of the specimen.

In this example, the pre-crack length $a = 20$ mm and width $w = 40$ mm are used. The uniform thickness of 1 mm is used, and the plane strain condition is considered. The linear hardening elastic-plastic material is utilized, and the material parameters are reported in Table 2. For elastic-plastic fracture analysis, the surface fracture energy $\Gamma_s = 33\text{KJ}/\text{m}^2$ is adapted.

In numerical peridynamic model, uniform mesh size is used. The proper grid size should be used to capture the elastic-plastic behaviors during crack growth. According to the fracture mechanic theory [52], the plastic zone size R_p ahead of the crack tip in the plane strain case, estimated based on the von Mises yield criterion, is:

$$R_p = \frac{K^2}{2\pi\sigma_Y^2} (1 - 2\nu^2) \quad (44)$$

where K is the stress intensity factor, σ_Y is the yield stress. Considering the material properties in Table 2 and the surface fracture energy Γ_s , the critical plastic zone size R_p for this CT specimen is equal to 1.0 mm. The mesh size of $\delta \leq R_p$ would be appropriate to fully capture the elastic-plastic behaviors during crack growth. And the δ -convergence and m -convergence studies are performed for further analysis. The process in Fig. 3 is implemented for elastic-plastic fracture analysis.

5.3.1. CT specimen with a stationary crack

First, the elastic-plastic behaviors of the CT specimen is analyzed with a stationary crack of $a = 20$ mm, linearly increasing displacement load $u(t)$ is symmetrically applied (see Fig. 20).

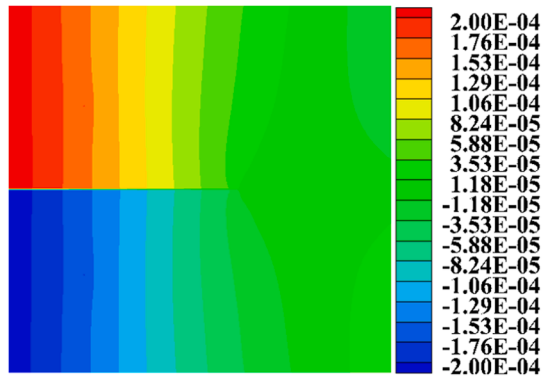
The distributions of equivalent Mises stress and equivalent plastic strain of the CT specimen at typical displacement loads of $u = 0.15$ mm and 0.3 mm are presented in Fig. 21, where the fixed values of $\delta = 1.0$ mm and $m = 4$ are utilized. As shown in Fig. 21, under the displacement load, the material plasticity happens not only around the crack tip, but also at loading areas and specimen right boundary. The plastic zone enlarges and connects together from crack tip to right boundary when $u = 0.3$ mm.

Additionally, the curve of applied force related to increasing displacement load is given in Fig. 22. As shown, the applied force nonlinearly increases with the displacement load because of the material elastic-plastic property. Meanwhile, the nonlinear energy release rate of the CT crack is presented in Fig. 23, where the ASTM standard equation in Eq. (41), and the extended PFCE model are, respectively considered. For the stationary crack, the values of nonlinear energy release rate is composed of the elastic and plastic components, where the plastic part increases rapidly and the elastic part tends to be flat after material yielding widely happens. Meanwhile, the J values from the ASTM equation and PFCE model are greatly consistent, with the maximum relative difference of 3.3 %.

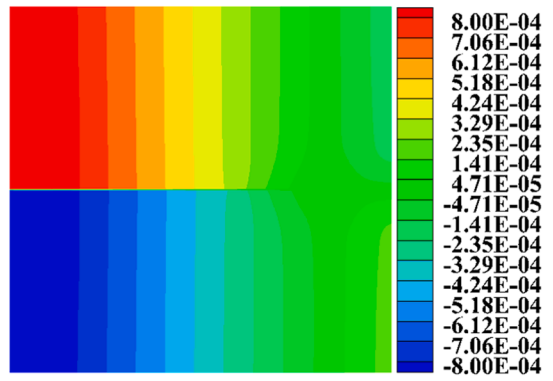
5.3.2. Elastic-plastic crack growth of CT specimen

The crack initiation and growth processes of CT test are then analyzed. The increasing displacement load is still considered, and the proposed energy dissipation rate-based bond failure criterion in Eq. (28) is utilized for elastic-plastic fracture analysis.

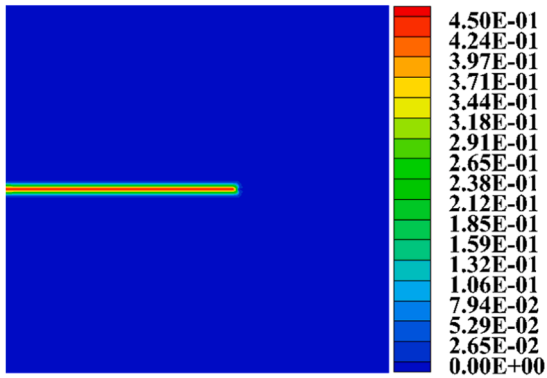
The distributions of y -direction displacement, crack path and equivalent plastic strain of the CT specimen at displacement loads of 0.2 mm and 0.8 mm are presented in Fig. 24. With the increasing displacement load, the crack starts to grow from the pre-crack tip (see Fig. 24(c)) and propagates along the pre-crack direction (see Fig. 24(d)). Meanwhile, the equivalent plastic strain appears around fresh



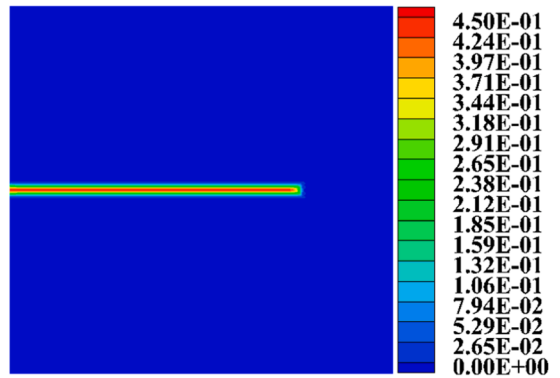
(a) $u = 0.2$ mm



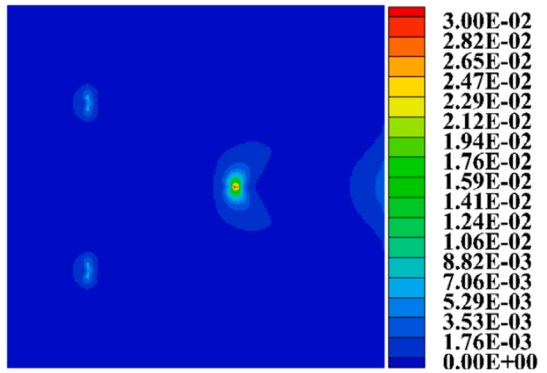
(b) $u = 0.8$ mm



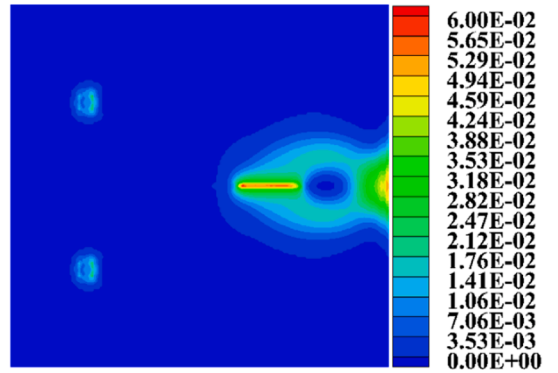
(c) $u = 0.2$ mm



(d) $u = 0.8$ mm



(e) $u = 0.2$ mm



(f) $u = 0.8$ mm

Fig. 24. Y-direction displacement (m) [(a) and (b)], local damage/crack path [(c) and (d)], and equivalent plastic strain [(e) and (f)] of the CT specimen under typical loads during crack growth.

crack surfaces, loading area and right boundary (see Figs. 24(e) and (f)). The crack grows with enlarging plastic zone, which is not only along the crack path, but also at right boundary and their middle areas (see Fig. 24(f)).

For quantitatively analysis, curves of different energy components changing with the displacement are shown in Fig. 25. As shown in Fig. 25, the summation of U_e (the strain elastic energy), U_p (the strain plastic energy), U_k (the kinetic energy), and W_S (the incremental surface energy) is equal to W_F (the work done by external forces) during the CT simulation, which is satisfied the energy conservation in Eq. (23) during this elastic-plastic fracture simulation.

Typically, the plots of elastic strain energy density, plastic strain energy density, surface energy density, and dissipation energy

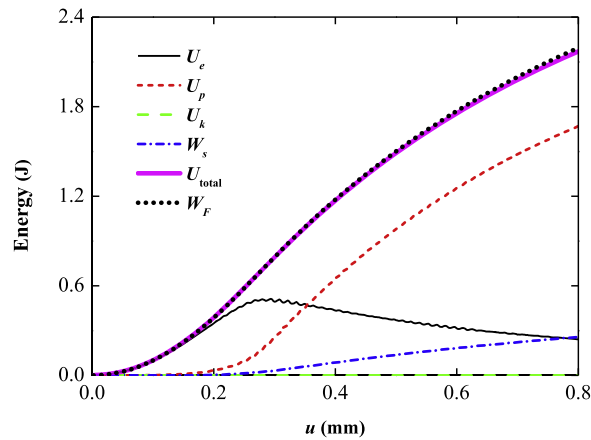


Fig. 25. Different energy components during the CT test simulation.

density of the CT specimen at typical loads of 0.28 mm and 0.6 mm are presented in Fig. 26. As shown, the elastic strain energy density is concentrated at the crack tip (see Fig. 26(a)), and moving with the crack tip (see Fig. 26(b)), which means unloading happens and the elastic energy releases after the crack passes by. The plastic strain energy density and released energy density irreversibly distribute around pre-crack tip and extend with the crack path, where the plastic strain energy density is widely distributed at plastic zone (see Fig. 26(c) and (d)), while the released energy density only appears along the fresh crack surfaces (see Fig. 26(e) and (f)). Additionally, the dissipation energy density, as the summation of released energy density and plastic strain energy, is also given for the total dissipated energy representation.

5.3.3. Convergence studies of elastic-plastic fracture

The δ -convergence and m -convergence studies are performed with varying horizon values of $\delta = 2.0$ mm, 1.0 mm and 0.5 mm, and of $m = 4, 5$ and 6. Since the analytical plastic zone size R_p is equal to 1.0 mm based on material properties, these horizon sizes also correspond to $2R_p$, R_p and $0.5R_p$.

First, the mesh sizes of $\delta = 2$ mm, 1 mm and 0.5 mm, and $m = 4$ are, respectively utilized for δ -convergence study. Distributions of equivalent plastic strain and dissipation energy density zoom-in at the plastic zone at displacement load of 0.6 mm are presented in Fig. 27. Generally, the plastic strain and dissipation energy distribute along the fresh crack surface, which reflects the leaving behind plastic wake. The horizon size has a great effect on elastic-plastic fracture behaviors. For the smaller horizon size, the crack extension length is shorter, and the maximum values of plastic strain and dissipation energy are much larger. Typically, when $\delta = 2R_p$, the plastic shape around the crack tip is not well modeled, the mesh size is too coarse to fully capture the elastic-plastic fracture behaviors.

Additionally, the applied force and crack growth length changing with displacement load during the CT simulation are, respectively presented in Figs. 28 and 29. As shown, the applied forces for different horizons are nearly coincided before crack growth, then decline at different points with different slopes during crack growth. For horizon sizes of $\delta \leq R_p$ ($\delta = 1$ mm, 0.5 mm), the ductile fracture behaviors are presented, the applied forces continue increasing even after crack initiation as $u = 0.2$ mm (compare Fig 28 and 29), then bend curvilinearly at the similar critical value, and slide down with different slopes; for the smaller grid size of $\delta = 0.5$ mm, the descending slope is lower. While as horizon size $\delta = 2R_p$ (2 mm), the fracture is approximately brittle, the applied force drops suddenly as crack starts to grow. Meanwhile, as shown in Fig. 29, the crack lengths for different horizon sizes are different, the crack grows more slowly for the smaller horizon size.

The incremental surface energy and plastic energy related to crack length for different horizon sizes are given in Fig. 30. For the different horizon sizes, the incremental surface energy curves are nearly coincided, and their slopes are closely equal to the standard surface fracture energy, which reflects the fracture energy equivalence during the elastic-plastic fracture. While the plastic energy is much larger for the smaller horizon size (see Fig. 30(b)), the CT fracture would experience more plastic deformation with the smaller horizon size.

Then, the mesh sizes of $\delta = 1$ mm, and $m = 4, 5$ and 6 are, respectively utilized for m -convergence study. The equivalent plastic strain and dissipation energy density zoom-in at the plastic zone are presented in Fig. 31. Overall, distributions of plastic strain and dissipation energy with different m are greatly consistent, the plastic wakes along the fresh crack surface are well captured. Meanwhile, the applied force changing with displacement load is given in Fig. 32, three curves for different values of m nearly coincide. The incremental surface energy and plastic energy during CT fracture are also given in Fig. 33. As presented, for different values of m , both the incremental surface energy and plastic energy are greatly consistent. The above figures all show that the value of m has small effect on elastic-plastic fracture behaviors.

Generally, the convergence studies show that the horizon size δ has a great effect on elastic-plastic fracture, more ductile behaviors would be presented for the smaller horizon size. And the mesh size of $\delta \leq R_p$ should be utilized to fully capture the elastic-plastic deformation during crack growth. While the value of m has small effect on elastic-plastic fracture, the CT fracture behaviors are greatly consistent for different values of m .

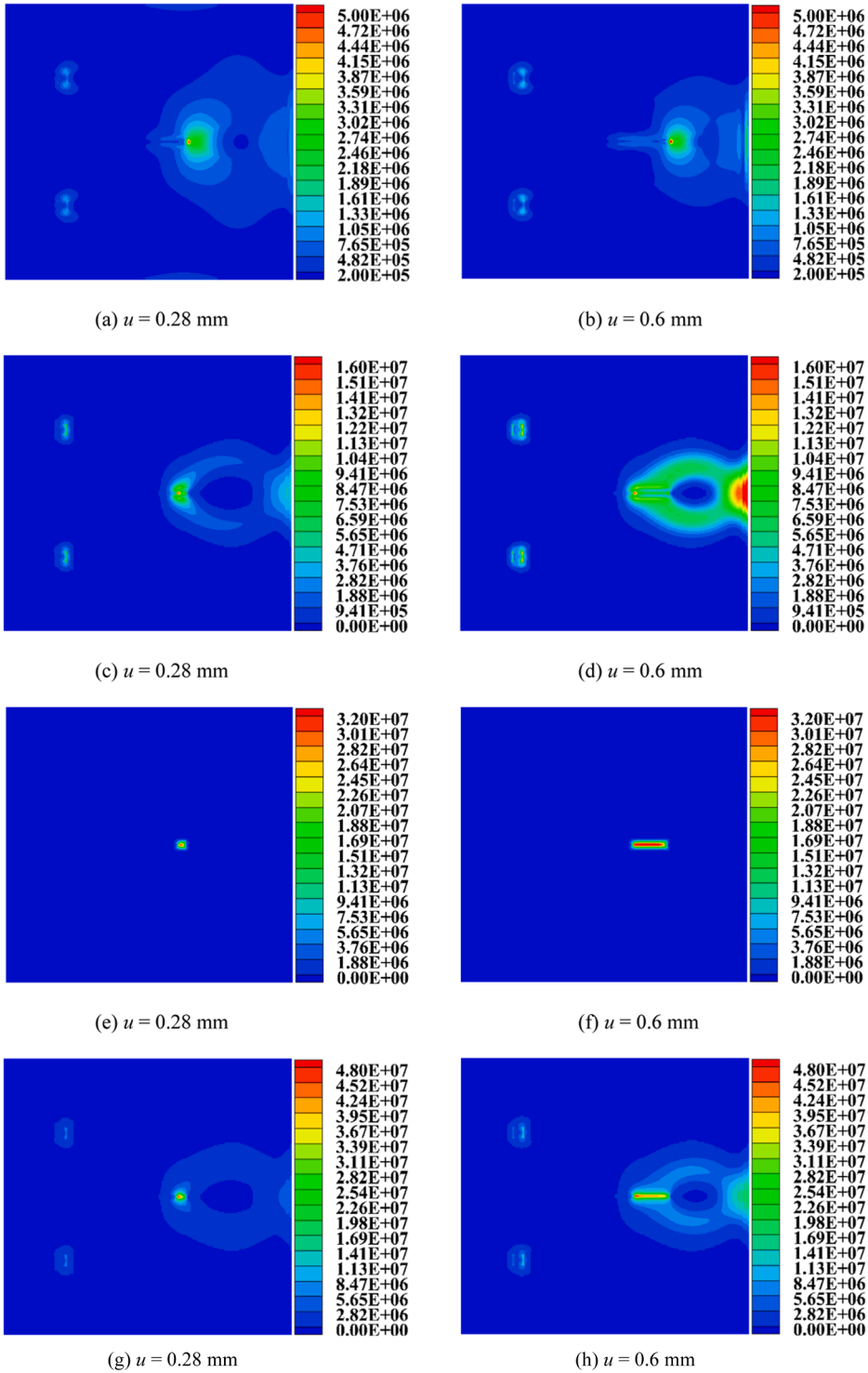


Fig. 26. Elastic strain energy density [(a) and (b)], plastic strain energy density [(c) and (d)], surface energy density [(e) and (f)], and dissipation energy density [(g) and (h)] under typical loads (J/m^3).

5.3.4. Resistance curves of the CT test

Then, the numerical resistance curve of the CT test simulation is computed. And two parameters, J -integral (J) and energy dissipation rate (R), are, respectively calculated for the J -resistance and R -resistance curves.

The J -resistance curves of the CT test with different values of m are presented in Fig. 34, where the J -integral values are computed in

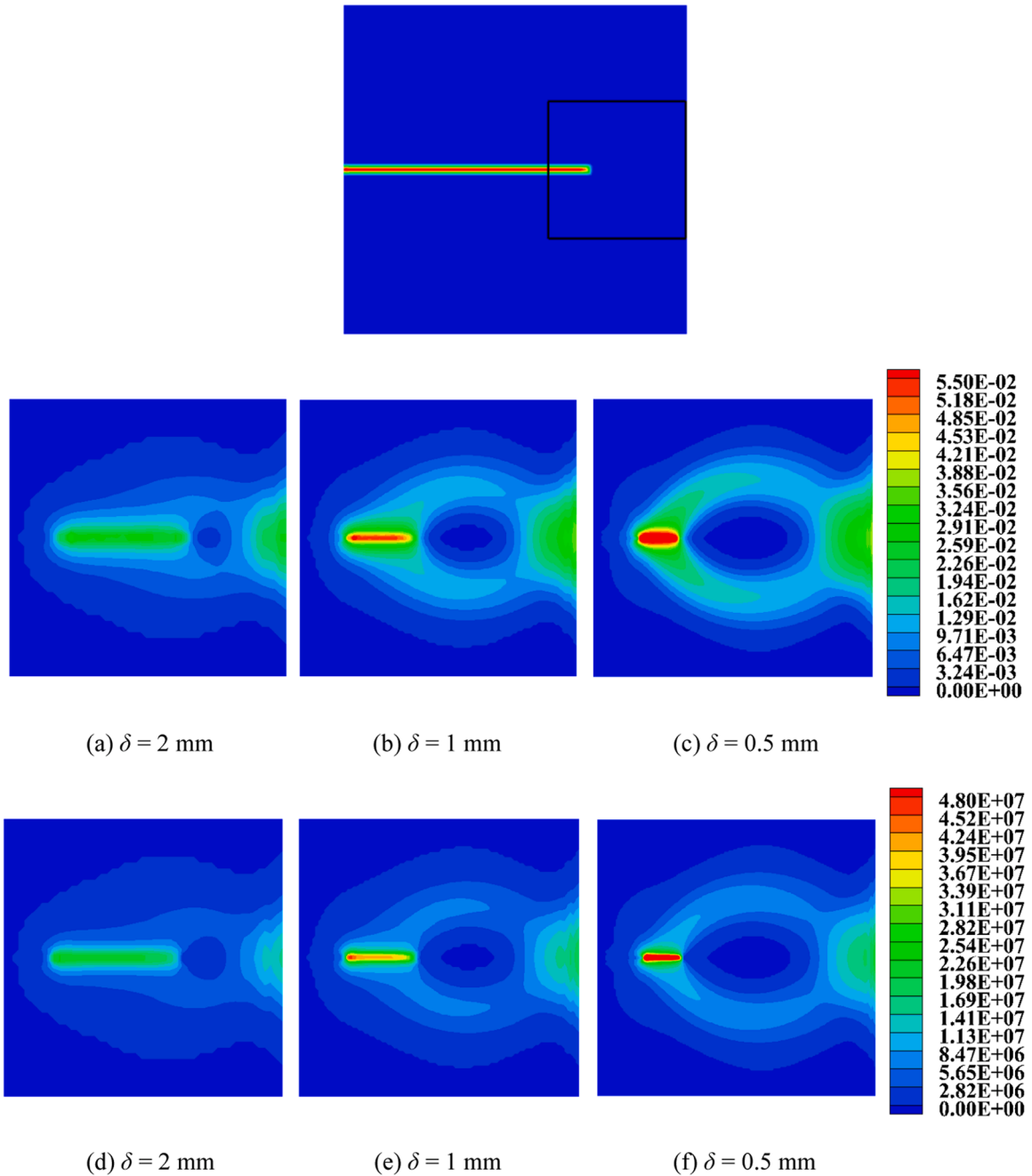


Fig. 27. Equivalent plastic strain [(a), (b) and (c)] and dissipation energy density (J/m^3) [(d), (e)] and (f) zoom-in at the plastic zone under $u = 0.6$ mm with the mesh sizes of $m = 4$, $\delta = 2$ mm, 1 mm and 0.5 mm.

Eq. (41) with the corresponding crack length. As shown, the J value rapidly increases at crack initiation state, and continues to increase with slower slope during crack stable propagation, which fits the tendency of typical J -resistance curve for ductile materials [44]. Meanwhile, the R -resistance curves during the CT fracture are given in Fig. 35, where the energy dissipation rate values are calculated in Eq. (26). As presented, the energy dissipation rate decreases with crack growth length, and would converge to a stable value.

6. Conclusions

In this paper, the peridynamics-based frame are proposed for the elastic-plastic fracture analysis. First, the peridynamic elastic-plastic models are proposed for elastic-plastic deformation and fracture analysis, the numerical strategy is presented for elastic-

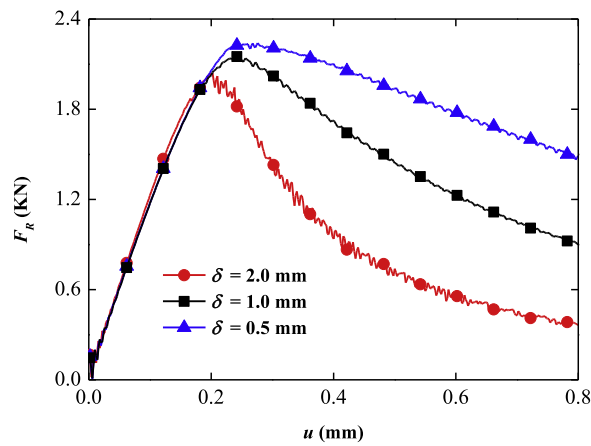


Fig. 28. Applied force versus displacement load for different values of δ .

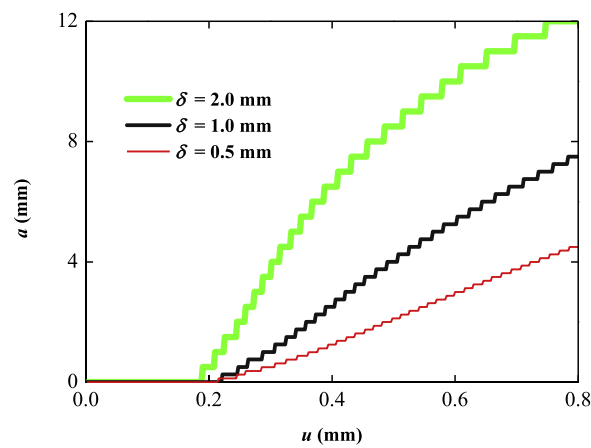


Fig. 29. Crack growth length versus displacement load for different values of δ .

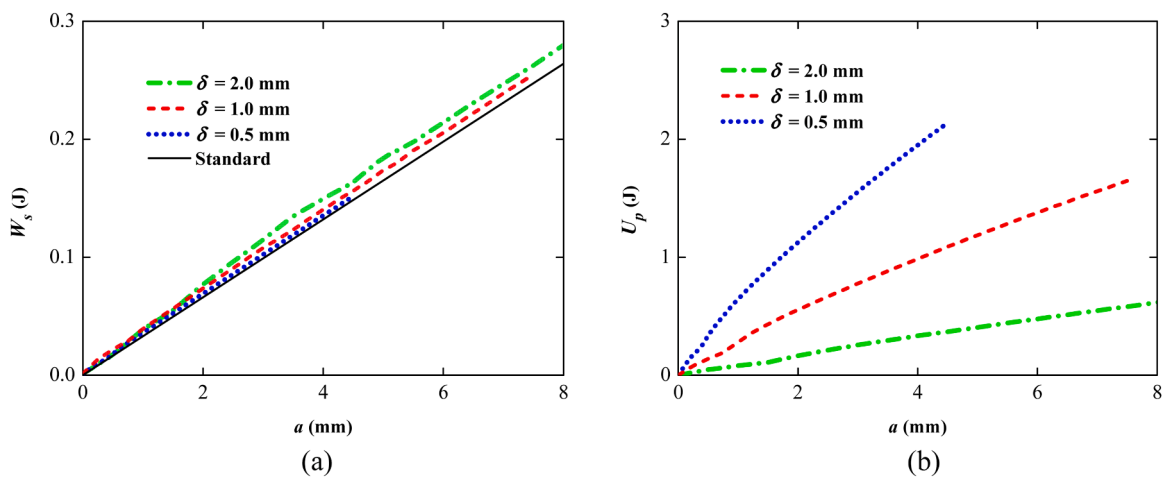


Fig. 30. Incremental surface energy (a) and plastic energy (b) versus crack growth length for different values of δ .

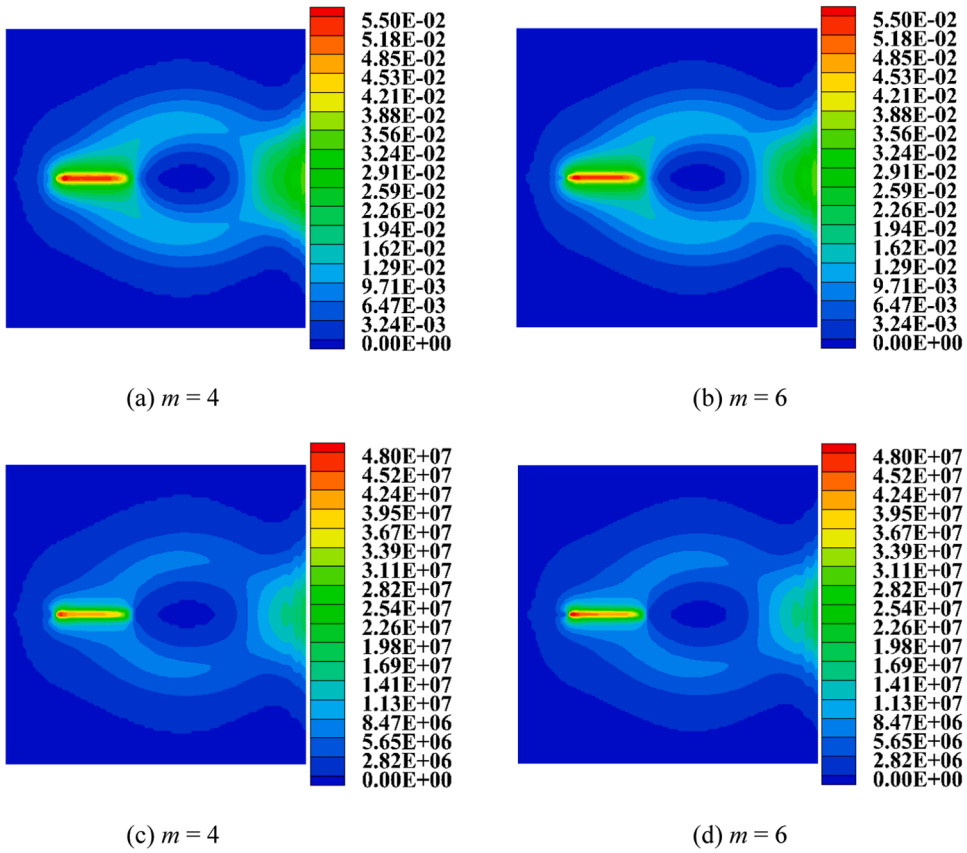


Fig. 31. Equivalent plastic strain [(a) and (b)] and dissipation energy density (J/m^3) [(c) and (d)] plots zoom-in at the plastic zone under $u = 0.6$ mm with the mesh sizes of $\delta = 1$ mm, $m = 4$ and $m = 6$.

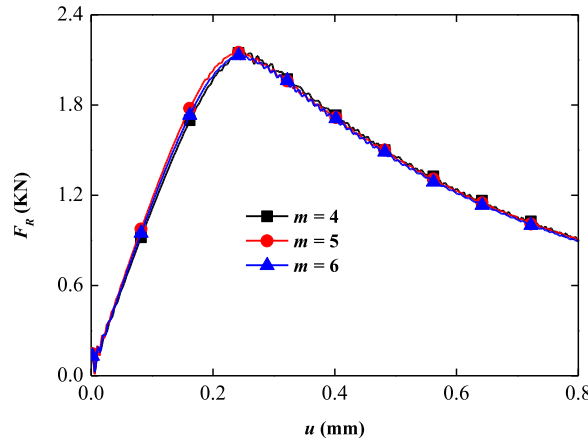


Fig. 32. Applied force versus displacement load for different values of m .

plastic numerical solution. Then, examples of plates with a center hole or a center crack and compact tension (CT) tests, are analyzed for the model verification and application.

In these numerical tests, the present peridynamic models can well capture the elastic-plastic deformation and fracture behaviors of specimens. The equivalent Mises stress, equivalent plastic strain and strain energy density of the plates are well presented, the loading and unloading behaviors are given. In the CT test, the nonlinear energy release rate J is computed with the ASTM equation and PFCE model, and they greatly match within the relative difference of 3.3 %. The crack initiation and growth processes of the CT test are analyzed with convergence studies. And the convergence studies show that the horizon size δ has a great effect on elastic-plastic

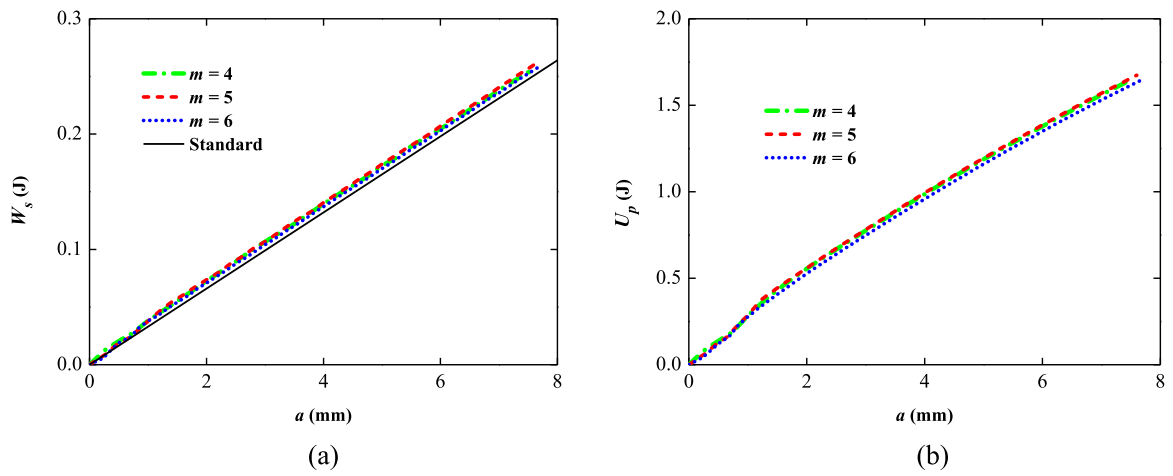


Fig. 33. Incremental surface energy (a) and plastic energy (b) versus crack growth length for different values of m .

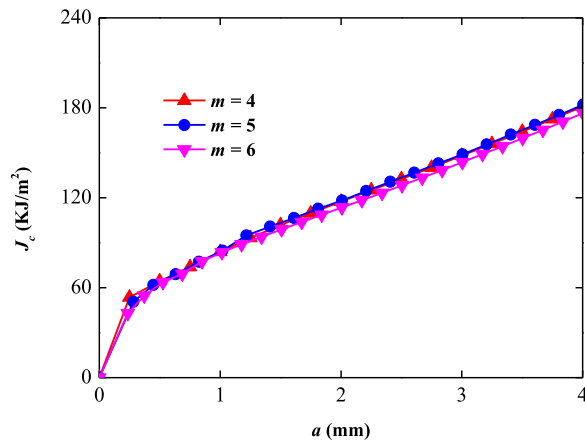


Fig. 34. J -resistance curves of the CT test.

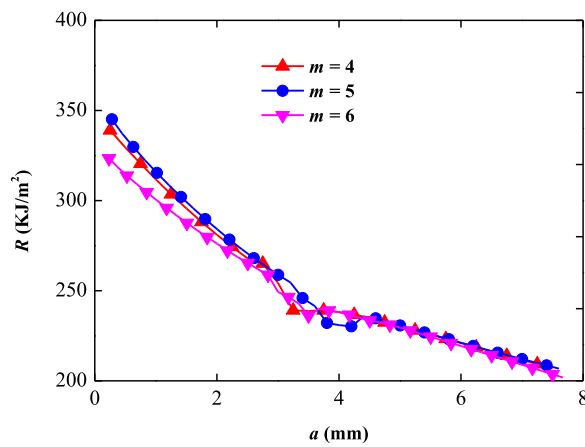


Fig. 35. R -resistance curves of the CT test.

fracture, while the value of m has small effect. More ductile behaviors would be presented for the smaller horizon size, and the horizon size of $\delta \leq R_p$ (plastic size) should be chosen.

In summary, the proposed peridynamics-based frame can well capture the elastic-plastic deformation and ductile fracture behaviors. With which the peridynamic theory can be applied for quantitatively analysis of ductile fracture and failure problems.

Declaration of Competing Interest

We declare that we have no known competing financial interests or personal relationships that could have appeared to influence the work entitled "Peridynamic modeling of elastic-plastic ductile fracture".

Data availability

No data was used for the research described in the article.

Acknowledgment

The financial supports from the National Natural Science Foundation of China (No. 12102226) are gratefully acknowledged.

References

- [1] J.R. Rice, G.F. Rosengren, Plane strain deformation near a crack tip in a power-law hardening material, *J. Mech. Phys. Solids* 16 (1968) 1–12.
- [2] J.W. Hutchinson, Singular behavior at the end of a tensile crack in a hardening material, *J. Mech. Phys. Solids* 16 (1968) 13–31.
- [3] C.E. Turner, A re-assessment of ductile tearing resistance, part I: the geometry dependence of J-R curves in fully plastic bending, in: *Eighth European Conference on Fracture*, EMAS, Warley, UK, 1990, pp. 933–949.
- [4] K.N. Shivakumar, J.H. Crews, Energy dissipation associated with crack extension in an elastic-plastic material, *Eng. Fract. Mech.* 28 (1987) 319–330.
- [5] D. Memhard, W. Brocks, S. Fricke, Characterization of ductile tearing resistance by energy dissipation rate, *Fatigue Fract. Eng. Mater. Struct.* 16 (1993) 1109–1124.
- [6] H. Li, N. Chandra, Analysis of crack growth and crack-tip plasticity in ductile materials using cohesive zone models, *Int. J. Plast.* 19 (2003) 849–882.
- [7] S. Dhar, P.M. Dixit, R. Sethuraman, A continuum damage mechanics model for ductile fracture, *Int. J. Press. Vessel. Pip.* 77 (2000) 335–344.
- [8] Z. Yang, An energy-based crack growth criterion for modelling elastic-plastic ductile fracture, *Mech. Res. Commun.* 32 (2005) 514–524.
- [9] F.P. Duda, A. Ciarbonetti, P.J. Sánchez, A.E. Huespe, A phase-field/gradient damage model for brittle fracture in elastic-plastic solids, *Int. J. Plast.* 65 (2014) 269–296.
- [10] Y. Jiang, C. Li, C. Wu, T. Rabczuk, J. Fang, A double-phase field method for mixed mode crack modelling in 3D elasto-plastic solids with crack-direction-based strain energy decomposition, *Comput. Methods Appl. Mech. Eng.* 405 (2023), 115886.
- [11] S.A. Silling, Reformulation of elasticity theory for discontinuities and long-range forces, *J. Mech. Phys. Solids* 48 (2000) 175–209.
- [12] S.A. Silling, E. Askari, A meshfree method based on the peridynamic model of solid mechanics, *Comput. Struct.* 83 (2005) 1526–1535.
- [13] S.A. Silling, M. Epton, O. Weckner, J. Xu, E. Askari, Peridynamic states and constitutive modeling, *J. Elast.* 88 (2007) 151–184.
- [14] T.L. Warren, S.A. Silling, A. Askari, O. Weckner, M.A. Epton, J. Xu, A non-ordinary state-based peridynamic method to model solid material deformation and fracture, *Int. J. Solids Struct.* 46 (2009) 1186–1195.
- [15] X. Gu, E. Madenci, Q. Zhang, Revisit of non-ordinary state-based peridynamics, *Eng. Fract. Mech.* 190 (2018) 31–52, <https://doi.org/10.1016/j.engfracmech.2017.11.039>.
- [16] H. Zhang, P. Qiao, A two-dimensional ordinary state-based peridynamic model for elastic and fracture analysis, *Eng. Fract. Mech.* 232 (2020), 107040.
- [17] Q.V. Le, W.K. Chan, J. Schwartz, A two-dimensional ordinary, state-based peridynamic model for linearly elastic solids, *Int. J. Numer. Methods Eng.* 98 (2014) 547–561.
- [18] S.R. Chowdhury, P. Roy, D. Roy, J.N. Reddy, A peridynamic theory for linear elastic shells, *Int. J. Solids Struct.* 84 (2016) 110–132.
- [19] J. O'Grady, J. Foster, Peridynamic plates and flat shells: a non-ordinary, state-based model, *Int. J. Solids Struct.* 51 (2014) 4572–4579.
- [20] J. O'Grady, J. Foster, Peridynamic beams: a non-ordinary, state-based model, *Int. J. Solids Struct.* 51 (2014) 3177–3183.
- [21] J.A. Mitchell, A non-local, ordinary state-based viscoelasticity model for peridynamics, *Albuquerque SAND2011–8064* (2011).
- [22] J.T. Foster, S.A. Silling, W.W. Chen, Viscoplasticity using peridynamics, *Int. J. Numer. Methods Eng.* 81 (2011) 1242–1258.
- [23] J.A. Mitchell, A nonlocal, ordinary, state-based plasticity model for peridynamics, *Albuquerque SAND2011–3166* (2011).
- [24] E. Madenci, S. Oterkus, Ordinary state-based peridynamics for plastic deformation according to von Mises yield criteria with isotropic hardening, *J. Mech. Phys. Solids* 86 (2016) 192–219.
- [25] H. Pashazad, M. Kharazi, A peridynamic plastic model based on von Mises criteria with isotropic, kinematic and mixed hardenings under cyclic loading, *Int. J. Mech. Sci.* 156 (2019) 182–204.
- [26] Lammi, T.J. Vogler, A nonlocal peridynamic plasticity model for the dynamic flow and fracture of concrete, *SAND2014–18257* (2014).
- [27] X.P. Zhou, T. Zhang, Q.H. Qian, A two-dimensional ordinary state-based peridynamic model for plastic deformation based on Drucker-Prager criteria with non-associated flow rule, *Int. J. Rock Mech. Min. Sci.* 146 (2021), 104857.
- [28] X. Zhou, T. Zhang, Generalized plastic ordinary state-based peridynamic model with shear deformation of geomaterials, *Acta Geotech.* 18 (2023) 609–623.
- [29] T. Zhang, X. Zhou, Q. Qian, The peridynamic Drucker-Prager plastic model with fractional order derivative for the numerical simulation of tunnel excavation, *Int. J. Numer. Anal. Methods Geomech.* 46 (2022) 1620–1659.
- [30] T. Zhang, X.P. Zhou, Q.H. Qian, Drucker-Prager plasticity model in the framework of OSB-PD theory with shear deformation, *Eng. Comput.* 39 (2023) 1395–1414.
- [31] F. Mousavi, S. Jafarzadeh, F. Bobaru, An ordinary state-based peridynamic elastoplastic 2D model consistent with J2 plasticity, *Int. J. Solids Struct.* 229 (2021), 111146.
- [32] M.M.M. Rahaman, P. Roy, D. Roy, J.N. Reddy, A peridynamic model for plasticity: micro-inertia based flow rule, entropy equivalence and localization residuals, *Comput. Methods Appl. Mech. Eng.* 327 (2017) 369–391.
- [33] A. Javili, A.T. McBride, J. Mergheim, P. Steinmann, Towards elasto-plastic continuum-kinematics-inspired peridynamics, *Comput. Methods Appl. Mech. Eng.* 380 (2021), 113809.
- [34] Y. Hu, G. Feng, S. Li, W. Sheng, C. Zhang, Numerical modelling of ductile fracture in steel plates with non-ordinary state-based peridynamics, *Eng. Fract. Mech.* 225 (2020), 106446.
- [35] J. Luo, V. Sundararaghavan, Stress-point method for stabilizing zero-energy modes in non-ordinary state-based peridynamics, *Int. J. Solids Struct.* 150 (2018) 197–207.

- [36] A. Yaghoobi, M.G. Chorzepa, Higher-order approximation to suppress the zero-energy mode in non-ordinary state-based peridynamics, *Comput. Struct.* 188 (2017) 63–79.
- [37] M. Asgari, M.A. Kouchakzadeh, An equivalent von Mises stress and corresponding equivalent plastic strain for elastic–plastic ordinary peridynamics, *Meccanica* 54 (2019) 1001–1014.
- [38] X.P. Zhou, Y.D. Shou, F. Berto, Analysis of the plastic zone near the crack tips under the uniaxial tension using ordinary state-based peridynamics, *Fatigue Fract. Eng. Mater. Struct.* 41 (2018) 1159–1170.
- [39] H. Zhang, P. Qiao, A state-based peridynamic model for quantitative fracture analysis, *Int. J. Fract* 211 (2018) 217–235.
- [40] J.T. Foster, S.A. Silling, W. Chen, An energy based failure criterion for use with peridynamic states, *Int. J. Multiscale Comput. Eng.* 9 (2011) 675–687.
- [41] Z. Liu, Y. Bie, Z. Cui, X. Cui, Ordinary state-based peridynamics for nonlinear hardening plastic materials' deformation and its fracture process, *Eng. Fract. Mech.* 223 (2020), 106782.
- [42] J.R. Rice, A path independent integral and the approximate analysis of strain concentration by notches and cracks, *J. Appl. Mech* 35 (1968) 379–386.
- [43] H. Zhang, P. Qiao, On the computation of energy release rates by a peridynamic virtual crack extension method, *Comput. Methods Appl. Mech. Eng.* 363 (2020), 112883.
- [44] T.L. Anderson, *Fracture Mechanics: Fundamentals and Applications* Edition (1995).
- [45] G.I. Taylor, H. Quinney, The latent energy remaining in a metal after cold working, in: *Proc. R. Soc. Lond.*, 143, 1934, pp. 307–326.
- [46] B. Kilic, E. Madenci, An adaptive dynamic relaxation method for quasi-static simulations using the peridynamic theory, *Theor. Appl. Fract. Mech.* 53 (2010) 194–204.
- [47] Q.V. Le, F. Bobaru, Surface corrections for peridynamic models in elasticity and fracture, *Comput. Mech.* 61 (2018) 499–518.
- [48] F. Bobaru, Y.D. Ha, Adaptive refinement and multiscale modeling in 2D peridynamics, *Int. J. Multiscale Comput. Eng.* 9 (2011) 635–660.
- [49] D. Yang, X. He, S. Yi, X. Liu, An improved ordinary state-based peridynamic model for cohesive crack growth in quasi-brittle materials, *Int. J. Mech. Sci.* 153–154 (2019) 402–415.
- [50] D. Behera, P. Roy, S.V.K. Anicode, E. Madenci, B. Spencer, Imposition of local boundary conditions in peridynamics without a fictitious layer and unphysical stress concentrations, *Comput. Methods Appl. Mech. Eng.* 393 (2022), 114734.
- [51] F. Bobaru, M. Yang, L.F. Alves, S.A. Silling, E. Askari, J. Xu, Convergence, adaptive refinement, and scaling in 1D peridynamics, *Int. J. Numer. Methods Eng.* 77 (2009) 852–877.
- [52] C.T. Sun, Z.H. Jin, *Fracture Mechanics*, Academic Press, Waltham, 2013.
- [53] ASTM, E1820-01: Standard test method for measurement of fracture toughness, 1996. *Annual Book ofASTM Standards*, vol. 03.01. West Conshohocken, PA: American Society for Testing and Materials; 2005.